

Early-Type Galaxies: Elliptical and S0 Galaxies, or Fast and Slow Rotators

Michele Cappellari^a

^aSub-Department of Astrophysics, Department of Physics, University of Oxford, Denys Wilkinson Building, Keble Road, Oxford, OX1 3RH, UK

Pre-print of a chapter for the Elsevier Encyclopedia of Astrophysics (edited by I. Mandel, section editor S. McGee)

Glossary

Elliptical galaxies (E) are galaxies with smooth, featureless light distributions and elliptical shapes, lacking spiral arms. They are denoted by ‘E’ followed by a number indicating their ellipticity.

S0 galaxies (lenticular galaxies) have a central bulge and a disk structure but lack the spiral arms characteristic of spiral galaxies.

Early-type galaxies (ETGs) comprise elliptical (E) and lenticular (S0) galaxies, or more meaningfully, are classified as fast or slow rotators based on their kinematic properties.

Fast-rotator ETGs are early-type galaxies with significant specific angular momentum, featuring stellar disks evident in their kinematics at any inclination. Extended disks appear as S0 galaxies when edge-on, while centrally concentrated disks with dominant spheroids are classified as disky ellipticals when edge-on. At low inclinations, fast rotators may be misclassified as ellipticals.

Slow-rotator ETGs are early-type galaxies with low specific angular momentum, typically spheroidal and lacking stellar disks. They are generally found above a critical stellar mass of $M_*^{\text{crit}} \approx 2 \times 10^{11} M_\odot$, or more accurately when $\lg(R_e/\text{kpc}) \gtrsim 12.4 - \lg(M_*/M_\odot)$. Slow rotators are classified as ellipticals regardless of orientation.

Supermassive black hole (SMBH) refers to black holes with masses ranging from $10^6 - 10^{10} M_\odot$, typically found at the centers of galaxies. Influences galaxy evolution through feedback mechanisms that regulate star formation.

Kinematically-decoupled stellar core (KDC) is a central region in a galaxy where the stars rotate in a different direction or at a different speed compared to the outer parts of the galaxy, often indicating past merger events

Integral-field Spectroscopy (IFS) is an observational technique that captures spatially-resolved spectral data across a galaxy, enabling two-dimensional mapping of kinematic and stellar population properties.

Line-of-sight velocity distribution (LOSVD) describes the range of velocities of stars or gas along the line of sight in a galaxy, providing insights into the galaxy’s kinematics and mass distribution.

Stellar initial mass function (IMF) is a function that describes the initial distribution of masses for a population of stars at the time of their formation, influencing the evolution of galaxies and the interstellar medium.

Half-light or effective radius (R_e) is the radius within which half of a galaxy’s total light is emitted. It is calculated as the radius of a circle with the same area as the galaxy’s half-light isophote.

Light-weighted second velocity moment (σ_e) is a kinematic parameter defined as $\sigma_e^2 \equiv \langle V^2 + \sigma^2 \rangle$, luminosity-weighted within the effective radius (R_e). Although often referred to as ‘effective velocity dispersion,’ σ_e combines contributions from both ordered stellar rotation (V) and random motions (σ).

Core density (Σ_1) is the stellar mass density within an aperture of radius $R = 1$ kpc, providing a measure of the central concentration of stars in a galaxy, which is related to its bulge mass fraction.

Specific angular momentum (λ_R) is a dimensionless parameter $0 \leq \lambda_R \leq 1$ that qualitatively measures the stellar angular momentum per unit mass in a galaxy. This parameter is typically calculated within the half-light isophote, R_e , and denoted as λ_{R_e} . It is defined by the equation: $\lambda_R = \langle R|V| \rangle / \langle R\sqrt{V^2 + \sigma^2} \rangle$, where R represents the radius, V is the rotational velocity, and σ is the velocity dispersion.

Fundamental Plane of galaxies is a relation connecting galaxies’ half-light radius (R_R), total luminosity (L), and second velocity moment (σ_e). Galaxies occupy a plane in the space defined by $(\lg R_e, \lg L, \lg \sigma_e)$ due to virial equilibrium and gradual variations in mass-to-light ratio (M/L) with σ_e .

Mass Plane of galaxies is a relation linking a galaxy’s mass (M), size (R_e), and second velocity moment (σ_e). Galaxies lie on a tight plane in the space defined by $(\lg R_e, \lg M, \lg \sigma_e)$, primarily due to virial equilibrium.

Virial mass estimator is a method to estimate the mass ($M \propto R_e \sigma_e^2$) or more accurately the mass-to-light ratio (M/L) within a given region of a gravitationally bound system using the virial theorem, relating the system’s total kinetic energy to its gravitational potential energy.

Galaxy environment refers to local conditions affecting galactic evolution, ranging from isolated fields to dense clusters and cosmic filaments.

Stellar metallicity is the abundance of elements heavier than hydrogen and helium, indicating the galaxy’s chemical composition and star formation history. Higher metallicity suggests multiple generations of star formation, enriching the interstellar medium with metals.

Stellar α enhancement refers to a higher ratio of α elements (like oxygen and magnesium) to iron, indicating a rapid, early star formation period. α elements are produced by Type II supernovae from massive stars (lifetime $< 5 \times 10^7$ yr), while iron is produced by Type Ia supernovae over longer timescales.

Galaxy quenching is the cessation of star formation in a galaxy due to environmental effects, internal feedback mechanisms, or gas depletion.

Galaxy clusters are vast structures containing hundreds to thousands of galaxies bound by gravity, embedded in dark matter and hot, X-ray-emitting gas. They are crucial for studying large-scale structure formation and galaxy evolution.

Abstract:

Early-type galaxies (ETGs) show a bimodal distribution in key structural properties like stellar specific angular momentum, kinematic morphology, and nuclear surface brightness profiles. Slow rotator ETGs, mostly found in the densest regions of galaxy clusters, become common when the stellar mass exceeds a critical value of around $M_*^{\text{crit}} \approx 2 \times 10^{11} M_\odot$, or more precisely when $\lg(R_e/\text{kpc}) \gtrsim 12.4 - \lg(M_*/M_\odot)$. These galaxies have low specific angular momentum, spheroidal shapes, and stellar populations that are old, metal-rich, and α -enhanced. In contrast, fast rotator ETGs form a continuous sequence of properties with spiral galaxies. In these galaxies, the age, metallicity, and α -enhancement of the stellar population correlate best with the effective stellar velocity dispersion $\sigma_e \propto \sqrt{M_*/R_e}$ (i.e., properties are similar for $R_e \propto M_*$), or with proxies approximating their bulge mass fraction. This sequence spans from star-forming spiral disks to quenched, passive, spheroid-dominated fast rotator ETGs. Notably, at a fixed σ_e , younger galaxies show lower metallicity. The structural differences and environmental distributions of ETGs suggest two distinct formation pathways: slow rotators undergo early intense star formation followed by rapid quenching via their dark halos and supermassive black holes, and later evolve through dry mergers during hierarchical cluster assembly; fast rotators, on the other hand, develop more gradually through gas accretion and minor mergers, becoming quenched by internal feedback above a characteristic $\lg(\sigma_e^{\text{crit}}/\text{km s}^{-1}) \gtrsim 2.3$ (in the local Universe) or due to environmental effects.

Key Points

- Early-type galaxies (ETGs) exhibit a bimodal distribution (two distinct peaks) in structural properties:
 - + Stellar specific angular momentum
 - + Kinematic morphology
 - + Nuclear surface brightness profiles
- The traditional E/S0 morphological classification fails to reflect this bimodality due to inclination-related observational biases
- A rotation-based classification (fast vs. slow rotators) provides a more physically meaningful framework:
 - + Slow rotators:
 - Primarily reside in dense regions of galaxy groups/clusters
 - Exhibit strong mass dependence: dominate above $M_*^{\text{crit}} \approx 2 \times 10^{11} M_\odot$
 - Sharper separation including half-light radii: $\lg(R_e/\text{kpc}) \gtrsim 12.4 - \lg(M_*/M_\odot)$
 - Features: Low specific angular momentum, spheroidal morphology, old/metal-rich/ α -enhanced stellar populations
 - + Fast rotators:
 - Host stellar disks and form a continuous sequence of physical properties with spiral galaxies
 - Stellar population properties (age, metallicity, α enhancement) best correlate with $\sigma_e \propto \sqrt{M_*/R_e}$
 - Implication: Population properties remain constant along $M_* \propto R_e$ lines in the (M_*, R_e) plane
 - σ_e empirically traces bulge mass fraction or central stellar density at fixed galaxy mass
 - Sequence ranges from star-forming disks (bulge-less) to quenched spheroid-dominated fast rotators
- Formation pathways differ markedly between the two classes:
 - + Slow rotators:
 - Early rapid star formation followed by quenching via dark halo/SMBH feedback
 - Growth via dry mergers during hierarchical assembly of host groups/clusters
 - + Fast rotators:
 - Gradual evolution through gas accretion and minor mergers
 - Quenching triggered by internal feedback, for $\lg(\sigma_e^{\text{crit}}/\text{km s}^{-1}) \gtrsim 2.3$, or environmental processes

1 Introduction

“What are galaxies? No one knew before 1900. Very few people knew in 1920. All astronomers knew after 1924” With this sentence, Allan Sandage opens his book *The Hubble Atlas of Galaxies*. The year 1924 marked a pivotal moment in astronomy with Edwin Hubble’s groundbreaking work, which convincingly demonstrated that galaxies are extragalactic objects. Today, a century later, we understand that galaxies are fundamental building blocks of the Universe. These cosmic structures, containing billions of stars, have sizes and masses comparable to the Milky Way galaxy.

The discovery that galaxies are ‘island Universes’ initiated their systematic study. As in many scientific fields, the first step involved classifying them to uncover regularities in their properties. Extending earlier, more rudimentary approaches (see a historical review by Sandage 2005), Edwin Hubble proposed a well-defined scheme for visually classifying galaxies based on optical images (Hubble 1926). Two major classes emerged: (i) Early-Type Galaxies (ETGs), characterized by their smooth, elliptical or lenticular shapes without spiral arms, and (ii) Spiral galaxies, defined by the presence of spiral arms traced by patchy dust and clumpy star-forming regions. In this chapter, focusing on ETGs, I consistently use Hubble’s morphological classification, which remains universally adopted, to distinguish them from spiral galaxies.

ETGs dominate the high-mass end of the galaxy mass distribution. In our current paradigm of galaxy formation, galaxies and their central

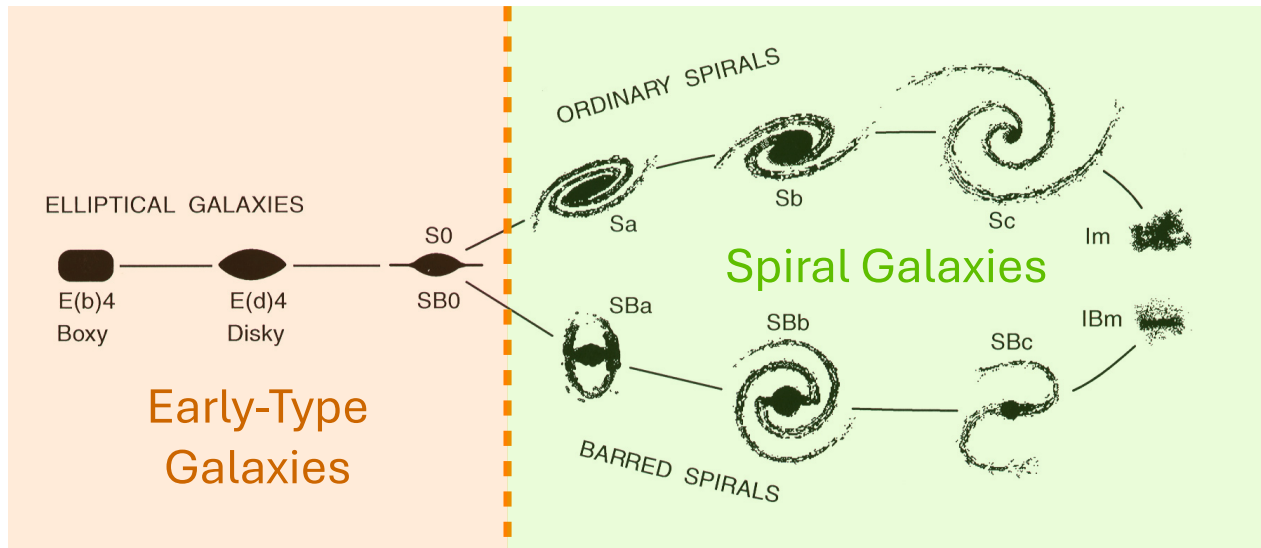


Fig. 1 Hubble's tuning-fork diagram for galaxy classification, adapted from Hubble (1936, pg. 45). The diagram features elliptical galaxies (E) along the handle, which then splits into two prongs representing spiral galaxies. The top prong depicts normal spirals (S), ranging from tightly wound, bulge-dominated types (Sa) to loosely wound, bulge-less types (Sc). The bottom prong shows barred spirals (SB), characterized by a bar-shaped structure and similar subclasses. Lenticular galaxies (S0), located at the fork's split, bridge the gap between elliptical and spiral galaxies, featuring a central bulge and disk but lacking prominent spiral arms. This version of the diagram was modified by Kormendy & Bender (1996) to include boxy E(b) and diskly E(d) elliptical galaxies, as well as irregular galaxies Im. I added annotations to differentiate early-type galaxies (E and S0), the focus of this chapter, from spiral galaxies.

supermassive black holes (SMBHs) grow hierarchically, starting from smaller building blocks and increasing in mass over time (White & Rees 1978; Blumenthal et al. 1984). This suggests that ETGs represent the end-point of galaxy and SMBH evolution. As such, they encode the full history of galaxy assembly and are ideal for studying galaxy formation and evolution. By examining ETG properties such as their stellar populations, kinematics, and chemical abundances, astrophysicists can reconstruct their formation and evolutionary histories.

Moreover, ETGs offer a unique laboratory for investigating how galaxies evolve through interactions with their surrounding environment. Processes like galaxy mergers, harassment, and ram pressure stripping can significantly impact ETG properties, providing clues about the environmental factors shaping their evolution.

This chapter provides a comprehensive overview of ETGs, exploring their defining characteristics, classification schemes, and fundamental properties. I will discuss their formation and evolution, considering both theoretical models and observational evidence. The impact of environmental factors on ETGs will also be discussed, highlighting the complex interplay between galaxies and their surroundings.

2 Photometric Properties

2.1 Morphological Classification from Images

The term 'early' in ETGs was inspired to Hubble by the evolutionary sequence proposed by Jeans (1928), who also presented a Y-shaped diagram to visually arrange morphological classes, a precursor to Hubble's tuning-fork. In the first published version of his classification, Hubble (1926) referred to all ETGs as 'elliptical' galaxies. Later, in Chapter II of the book where he presented his classification tuning fork (Hubble 1936), he introduced S0 galaxies as a "hypothetical class" intermediate between elliptical and spiral galaxies.

Hubble classified elliptical galaxies (Es) based on their apparent axial ratio. Ellipticity is defined as $\varepsilon = 1 - b/a$, where a and b are the major and minor axes of the galaxy isophotes, respectively. Hubble defined the position in the E sequence by estimating the ellipticity to one decimal point, omitting the point (e.g., an elliptical with $\varepsilon \approx 0.32$ is classified as E3). Hubble later recognized that variations in elliptical galaxies could not be described by ellipticity alone, and that Es needed to be separated into (i) ellipticals (E), with elliptical isophotes, and (ii) S0 galaxies, with lenticular shapes flatter than E7 but no evidence of spiral arms. This revised Hubble classification, still universally adopted today, was published after his death by his collaborator Allan Sandage (Sandage 1961). Figure 1 presents Hubble's tuning fork, with the ETGs part of the diagram modified by Kormendy & Bender (1996) to account for key differences in the elliptical class.

Spiral galaxies are characterized by the presence of a stellar disk and spiral arms. At the center of the disk, they contain a stellar spheroid or 'bulge' which somewhat resembles a very flattened E galaxy. Hubble classified spiral galaxies as Sa, Sb, and Sc according to the prominence of the bulge, with Sa being the most bulge-dominated. He also noted that more bulge-dominated spirals have more closely coiled spiral arms and used this as an additional criterion in his classification.

Later, van den Bergh (1976) noted that S0 galaxies can span the full range of bulge fractions as spiral galaxies. He proposed a revision

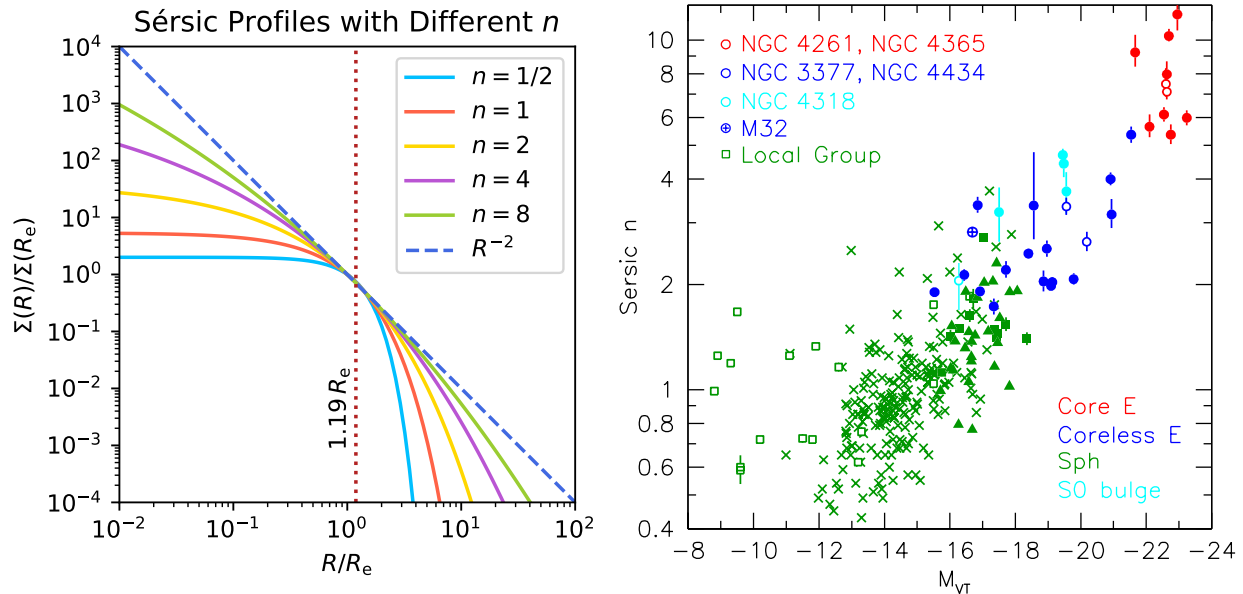


Fig. 2 Left panel: Sérsic profiles of Equation (1) for different logarithmically-spaced values of the Sérsic index n . All profiles have the same logarithmic slope $\gamma = -2$ at a radius $R \approx 1.19R_e$, indicated by the vertical dotted line with 1% accuracy, where R_e is the half-light radius. The dashed line shows the asymptotic profile $\Sigma \propto R^{-2}$ for $n \rightarrow \infty$. Right panel: Correlation between Sérsic index n and visual magnitude M_{VT} . Red, blue, green, and cyan points represent core ellipticals (Es), non-core ellipticals, spheroidal galaxies, and S0 bulges, respectively. Green triangles, crosses, and open squares indicate spheroidals (Kormendy et al. 2009, fig. 33).

of Hubble’s classification by adding a small letter to S0 galaxies, like S0a, S0b, and S0c, to qualitatively indicate their bulge fraction. He suggested a trident to replace the tuning fork, with the S0s in one of the arms like the spirals, to highlight the parallelism between spiral and S0 galaxies. A problem with this classification is that S0 galaxies are not easy to distinguish from E galaxies unless seen close to edge-on, because bulges become hard to recognize from the stellar disk. Bulge fractions of S0s are even more difficult to visually assess at low inclination ($i = 90$ being edge-on).

Although the distinction between early-type and spiral galaxies is based on visual images alone, the two types differ by various other characteristics, indicating that the classification is physically meaningful. ETGs appear smooth because they have lower amounts of gas and star formation than spiral galaxies. Therefore, their stellar population is generally older and they have redder colors. However, a separation based on color or ages is not fully equivalent to one based on morphology and cannot be used interchangeably (Strateva et al. 2001).

2.2 Global Surface Brightness Profiles

Early quantitative measurements of the surface brightness profiles $\Sigma(R)$ of ETGs, obtained from digitized photographic plates, initially suggested that they could be universally described by an $R^{1/4}$ function when expressed in magnitudes $\mu = -2.5 \lg(\Sigma/\Sigma_0)$ (de Vaucouleurs 1948). However, later observations, leveraging the development of CCD detectors, revealed that these profiles were not universal. Instead, they required a more general function proposed by Sérsic (1968):

$$\Sigma(R) = \Sigma_e \exp \left\{ -b_n \left[\left(\frac{R}{R_e} \right)^{1/n} - 1 \right] \right\}, \quad (1)$$

This function reduces to the de Vaucouleurs profile when $n = 4$. Here, R_e represents the radius enclosing half of the total galaxy luminosity integrated from the analytic profile, $\Sigma_e \equiv \Sigma(R_e)$, and $b_n = Q^{-1}(2n, 1/2)$ is a normalization factor designed to satisfy the R_e definition, with Q^{-1} the inverse of the regularized incomplete gamma function (Olver et al. 2010, eq. 8.2.4), which is available in most popular programming languages¹ (Kai Zhu et al. in preparation).

Qualitatively, as n increases, the galaxy light at radii around R_e is redistributed to both smaller and larger radii (see Figure 2). A large n indicates a galaxy with both (i) a more concentrated light distribution in the central regions and (ii) a more extended stellar halo at larger radii. In the limit as $n \rightarrow \infty$, the Sérsic profile tends to a power law $\Sigma(R) \propto R^{-2}$. As n increases, a larger fraction of the total luminosity of the Sérsic profile is distributed to larger radii, where the surface brightness can fall below observable levels. This makes the empirical determination of R_e less accurate for galaxies with large n . Figure 2 also shows that the variation of the Sérsic profiles is nearly uniform when n is sampled logarithmically. Therefore, correlations involving the Sérsic index are better studied using $\lg n$ instead of n , to avoid the ‘saturation’ of profile variations at large n .

¹E.g., in Python `scipy.special.gammaincinv`, or in Mathematica `InverseGammaRegularized`.

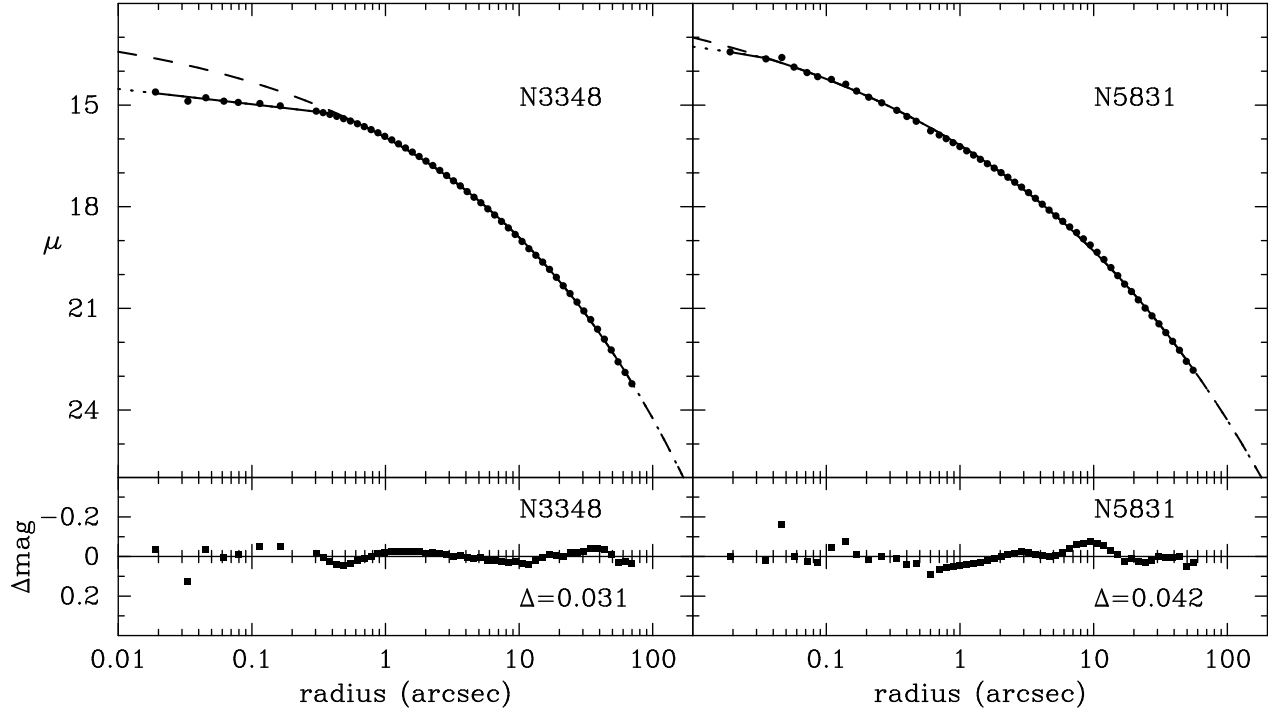


Fig. 3 HST major-axis surface brightness profiles of elliptical galaxies. The solid lines represent fits using Equation (2), with dotted lines showing inner and outer extrapolations, and dashed lines indicating inward extrapolations of the Sérsic-like component beyond the break radius. For NGC 5831, the best fit is nearly a pure Sérsic model. In contrast, NGC 3348 (classified as a ‘core’ galaxy) exhibits a distinct inner break. The root-mean-square (rms) scatter Δmag for each fit is provided below the corresponding panel (Graham et al. 2003, fig. 10).

As shown in Figure 2, the half-light radius R_e is close to the radius R_2 at which the Sérsic profiles have the logarithmic slope $\gamma = -2$ of the asymptotic profile. More precisely, $R_2/R_e \approx 1.19$ with better than 1% accuracy for all realistic values of n . For a Gaussian ($n = 1/2$ in Equation (1)), $R_2/R_e = 1/\sqrt{\ln(2)} \approx 1.201$, and this ratio monotonically decreases with a minimum value $\lim_{n \rightarrow \infty} R_2/R_e = e^{1/6} \approx 1.181$.

The importance of Sérsic profiles lies not just in providing better fits to galaxy surface brightness. More importantly, n correlates with galaxy properties, with brighter and larger galaxies having larger n (Caon et al. 1993). Figure 2 illustrates the correlation between galaxy luminosity and n as derived by Kormendy et al. (2009). This trend indicates that the Sérsic index contains information on galaxy evolution, as I will discuss later.

A single Sérsic profile generally does not describe S0 galaxies well, as they often consist of a bulge and a disk component like spiral galaxies. In these cases, the disks are generally described by exponential profiles ($n = 1$ in Equation (1)) like those of spirals (Freeman 1970), and only the bulge has a free Sérsic index n .

2.3 Nuclear Surface Brightness Profiles

With the launch of the Hubble Space Telescope (HST) in 1990, it became possible to measure galaxy surface brightness profiles at radii smaller than the atmospheric seeing limit, which typically blurs point-like stars to about 1 arcsecond in size (full-width at half-maximum, FWHM). Observations revealed that the surface brightness profiles of ETGs continue to increase as a power law $\Sigma(R) \propto R^{-\gamma}$ down to the HST’s spatial resolution limit. However, some galaxies exhibited a nuclear break with a sharp change in the logarithmic slope γ inside the break radius (Ferrarese et al. 1994; Lauer et al. 1995).

The nuclear surface brightness profiles can be described using either double power-laws (Lauer et al. 1995) or the Core-Sérsic parametrization (Graham et al. 2003; Trujillo et al. 2004):

$$\Sigma(R) = \Sigma' \left[1 + \left(\frac{R_b}{R} \right)^\alpha \right]^{\gamma/\alpha} \exp \left[-b_n \left(\frac{R^\alpha + R_b^\alpha}{R_e^\alpha} \right)^{1/(\alpha n)} \right]. \quad (2)$$

Outside the inner break at radius $R = R_b$, this is a Sérsic (1968) profile with a projected half-light radius R_e , but it gradually transitions to a power-law surface brightness $\Sigma(R) \propto R^{-\gamma}$ at smaller radii $R \ll R_b$. The exponent α controls the sharpness of the break, while Σ' is the overall normalization. Figure 3 shows an application of this profile to a real galaxy and illustrates the difference between core/deficit galaxies and pure Sérsic galaxies.

The behavior of the nuclear surface brightness is strongly related to the galaxy’s total luminosity. Luminous galaxies with absolute total V-band magnitudes $M_V \lesssim -22$ have a core, characterized by a sharp break from a steep outer profile to a much shallower inner profile with

$\gamma \lesssim 0.3$. The core can also be described as a light *deficit* relative to a Sérsic profile and quantified using the profile in Equation (2). At lower luminosities, galaxies have inner surface brightness profiles described by a Sérsic profile, with some overlap in the transition region (e.g., Faber et al. 1997). The fact that bright ETGs possess both a large Sérsic index and a core/deficit in their nuclei is illustrated in Figure 2.

2.4 Isophotal Shapes

With the advent of CCD detectors in the 1980s, it became possible to analyze the detailed shape of the isophotes of elliptical galaxies. It was discovered that some of these galaxies were not well approximated by pure ellipses. Instead, they had more disky, or almond-shaped, isophotes. This was interpreted as indicating the presence of stellar disks, which were not as prominent as the disks of S0 galaxies and could only be detected as deviations of their isophotes from ellipses (Bender 1988).

Bright galaxies, unlike fainter ones, lacked disky isophotes, contained cores in their inner profiles, and exhibited slow rotation (section 3). This was deemed significant enough to propose a revision of Hubble’s tuning-fork diagram. Kormendy & Bender (1996) suggested that there was a continuous sequence from S0 galaxies to disky ellipticals, while brighter ETGs with cores constituted a distinct class of objects. They proposed using isophotal shape in galaxy classification, and their revised tuning-fork diagram is shown in Figure 1.

There was a crucial practical issue with the proposed classification: the presence of stellar disks in ellipticals could only be revealed by the shape of their isophotes when galaxies were close to edge-on ($i \approx 90^\circ$). Disky ellipticals would display elliptical isophotes in projection at lower inclinations. This limitation prevented the application of the proposed scheme on a galaxy-by-galaxy basis. This inclination dependence was the same issue that hindered the practical application of the S0a–S0c scheme proposed by van den Bergh (1976). As I will show in the next section, a solution to the inclination dependence of photometric classification schemes is provided by stellar kinematics obtained with integral-field spectroscopic observations.

3 Kinematics and Dynamics

3.1 Kinematic Morphology

The beginning of this century saw the emergence of integral-field spectroscopic (IFS) observations of galaxies. This allowed astrophysicists to obtain spectra over a contiguous two-dimensional region on the sky, fully covering the central regions of the galaxies, typically out to about $1R_e$, where the surface brightness is sufficiently large.

Similar to photometry, the first step after observing a statistically significant sample of galaxies with IFS was to visually classify the kinematic maps. All the maps of ETGs could be divided into five main classes introduced by Krajnović et al. (2011, table 3) and illustrated in Figure 4. The classification relies on the visual appearance of the maps, not the amplitude of the rotation.

- (a) **No rotation:** Galaxies showing barely detectable rotation at the typical accuracy level ($\sim 5 \text{ km s}^{-1}$) of good stellar kinematic measurements. The kinematic maps of these galaxies appear noisy when scaled to the maximum/minimum range of values.
- (b) **Complex rotation:** Galaxies presenting some clear, organized, and point-symmetric rotation with twists in the stellar kinematics, without a clearly defined symmetry axis in the kinematic map.
- (c) **Kinematically-decoupled core:** Galaxies rapidly rotating only inside a restricted central region, significantly smaller than $\sim 1R_e$. This inner kinematic core is decoupled from the rest of the galaxy, which generally rotates little, similar to classes (a) or (b).
- (d) **Counterrotating disks:** Galaxies showing rotation extending well beyond $1R_e$, with a symmetry axis coinciding with the photometric one but with a reversal of the sense of rotation inside $1R_e$. These galaxies can be explained by the presence of two counterrotating disks. The velocity reversal produces a region with nearly zero velocity on the map, where the two opposite velocities counterbalance. When the kinematics is extracted by modeling the line-of-sight velocity distribution (LOSVD) with a single Gaussian, the two opposite velocities appear as an increase of σ , which appear as two peaks in the velocity dispersion σ on opposite sides of the galaxy nucleus.
- (e) **Disk-like rotation:** Galaxies with regular velocity extending well outside $1R_e$ and with the same symmetry axes as the photometry. The velocity field is generally accurately described by that of a thin rotating disk, with a characteristic $\cos \theta$ (with θ the eccentric anomaly) variation along similar concentric ellipses.

3.2 Intrinsic Shapes

Measuring the intrinsic shapes of ETGs is challenging because we only observe their projection on the plane of the sky, and they lack the dusty spiral arms that could trace the equatorial plane. Even if we assume ETGs have density distributions approximately stratified on similar triaxial spheroids, with intrinsic axial ratios p and q , the two-dimensional distribution $f(p, q)$ of the intrinsic axial ratios cannot be inferred from the observed one-dimensional distribution of observed axial ratios $f(q')$. With IFS observations, we can additionally measure the distribution of the kinematic misalignment angle:

$$\Psi_{\text{mis}} = \text{PA}_{\text{kin}} - \text{PA}_{\text{phot}}, \quad (3)$$

which is the difference between the photometric major axis PA_{phot} and the kinematic major axis PA_{kin} . The definition of these angles is illustrated in Figure 5 for eight regular-rotator ETGs (kinematic-morphology class [e] in Figure 4). I measured the PA_{phot} with the

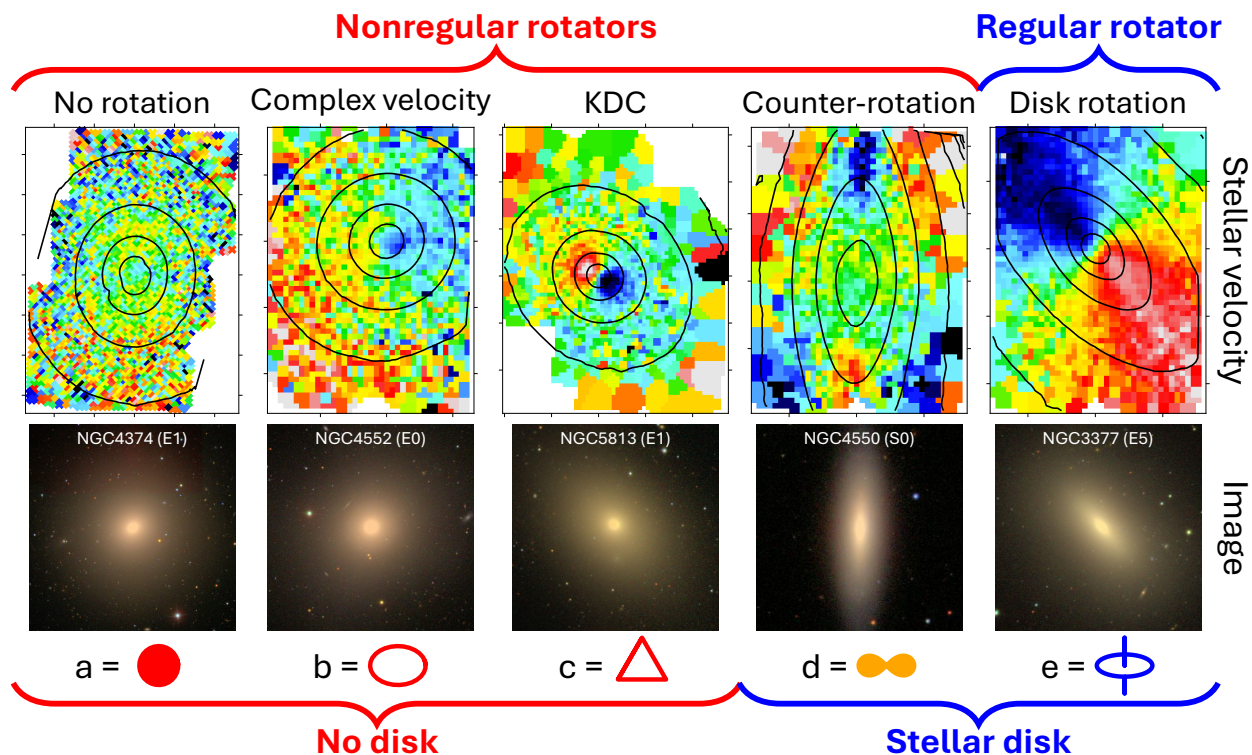


Fig. 4 Morphological classifications based on stellar kinematics. Early-type galaxies are divided into five classes as defined by Krajnović et al. (2011): (a) no detectable rotation, (b) nonregular rotation, (c) kinematically distinct cores (KDCs), (d) counter-rotating disks, and (e) regular disk-like rotation. The kinematic data, obtained from Emsellem et al. (2004), were spatially binned using the Voronoi tessellation method of Cappellari & Copin (2003). Tick marks on the images are spaced at 10 arcsecond intervals. The bottom row displays corresponding SDSS images, with Hubble’s morphological classifications indicated in parentheses next to the galaxy names. Classes (d) and (e) are physically related, as both feature stellar disks and are nearly axisymmetric, while the other classes show no evidence of stellar disks. Class (e) is labeled as regular rotators, whereas the remaining classes are classified as nonregular rotators. The symbols below the images represent the different morphological classes and are also used in Figure 6 and Figure 12.

`find_galaxy` function of the `mgefit` package² (Cappellari 2002) and the PA_{kin} with the `fit_kinematic_pa` function of the `pafit` package³ (Krajnović et al. 2006, appendix C). Note that stellar kinematics can generally be measured to much smaller radii than photometry. However, by comparing PA_{kin} within $1R_e$ against PA_{phot} measured at large radii, we can study the shapes of the outer stellar halos.

Unfortunately, adding the kinematic misalignment angle does not reduce the degeneracy of the problem because we do not know the misalignment angle between the angular momentum vector and the rotation axis of the galaxy. The angular momentum vector can lie anywhere in the plane containing the major and minor axes of the triaxial ellipsoid.

The issue may seem unsolvable in principle. However, when the first statistically significant sample of galaxies was observed, it was found that the kinematic misalignment for regular rotators tended to be small and nearly consistent with zero within measurement errors (see Figure 5 and Figure 6). The lack of kinematic misalignment for a significant sample of galaxies, out to their stellar halos, can only occur if these galaxies, as a class, are approximately axisymmetric (Krajnović et al. 2011; Graham et al. 2018). They are as axisymmetric as spiral galaxies (Barrera-Ballesteros et al. 2015). Most observed deviations from axisymmetry are consistent with the presence of bars, disturbances due to mergers, or lower-quality data. A statistical inversion of the intrinsic shapes of fast rotators was performed by Weijmans et al. (2014).

The situation is dramatically different for non-regular rotators, which tend to be relatively round in projection $\varepsilon \lesssim 0.4$. They show almost no preferred kinematic misalignment angle. This is partly due to their near lack of rotation, making PA_{kin} extremely unreliable. However, genuine and significant kinematic misalignment is observed in several non-regular rotators, indicating they must be triaxial. Their rather small maximum observed ellipticity indicates that they are at most weakly triaxial and quite close to spherical, with axial ratios $p > q \gtrsim 0.6$. A detailed statistical inversion of the shape of slow rotators was done by Li et al. (2018a).

Counter-rotating disks (kinematic-morphology class [d] in Figure 4) are an exception. They are closely related to regular-rotators due to the presence of stellar disks, which explains their flattened shapes.

²<https://pypi.org/project/mgefit/>

³<https://pypi.org/project/pafit/>

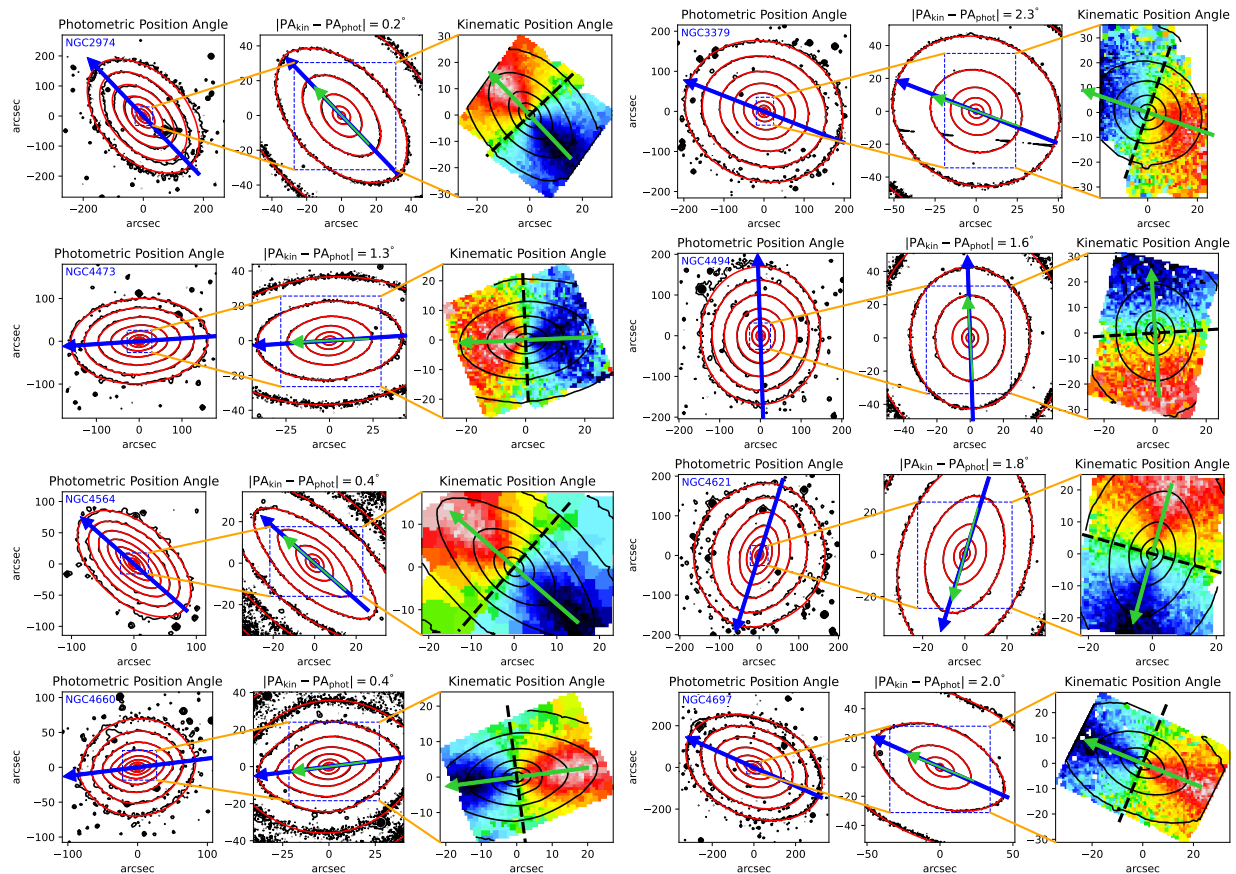


Fig. 5 Fast-rotator early-type galaxies (ETGs) are axisymmetric out to large radii: For each of the eight galaxies, the left and middle panels show the SDSS surface brightness contours (in black) at two different scales for regular rotator galaxies classified as ellipticals. The red contours represent a Multi-Gaussian Expansion (MGE) fit using `mge.fit_sectors` (Cappellari 2002), assuming a fixed photometric position angle (PA_{phot}) at all radii. The PA_{phot} , determined using `mge.find_galaxy`, is indicated by blue arrows. The close match between the observed images and the MGE fit confirms that the photometry is consistent with a constant PA_{phot} across all radii, with no detectable photometric twists. This behavior contrasts with triaxial systems, where radial ellipticity variations typically cause PA_{phot} twists. The right panel displays stellar kinematic maps (from Cappellari et al. 2011a) and the best-fitting kinematic position angle (PA_{kin}), measured using `pafit.fit_kinematic_pa` (Krajnović et al. 2006). In all cases, the kinematic misalignment is $|\Psi_{\text{mis}}| \leq 2^\circ$, within measurement uncertainties. The absence of PA_{phot} variation and the negligible Ψ_{mis} indicate that these galaxies maintain axisymmetry out to at least $4R_e$, the extent of the photometric data. These eight galaxies are representative of regular-rotator ETGs as a class, unless barred or otherwise disturbed.

3.3 Dynamical Modeling and Orbital Anisotropy

For external galaxies (excluding the Milky Way or some very nearby local-group galaxies), we can only measure line-of-sight velocities of their stars. This means the largest amount of dynamical information we can extract from a galaxy is a three-dimensional distribution, specifically the LOSVD at every spatial location on the galaxy image. For a fixed gravitational potential, the dynamics of a steady-state galaxy are fully described by the three-dimensional distribution function (DF), which is a function of the three isolating integrals of motion (e.g., Binney & Tremaine 2008, sec. 4.2). This implies that if (i) we knew the gravitational potential, and (ii) the galaxy was edge-on to avoid the mass deprojection degeneracy, one could theoretically invert the DF from the observed kinematics. However, these conditions are never fully satisfied for real observations of distant galaxies, leading to inherent degeneracies in modeling results.

Three main techniques have been used to model the stellar dynamics of ETGs, to understand their orbital distribution and the distribution of their mass content:

Jeans Modeling: Based on the moments of the collisionless Boltzmann equations, first applied to galaxies by Jeans (1922). It describes stars like an incompressible fluid in phase space moving under the influence of gravity and computes a prediction for the velocity moments, which are then fitted to the observed kinematics.

Orbital-Superposition Technique: Proposed by Schwarzschild (1979). It computes all possible orbits in a fixed gravitational potential and then finds the linear combination of those orbits that best fits the galaxy kinematics and photometry.

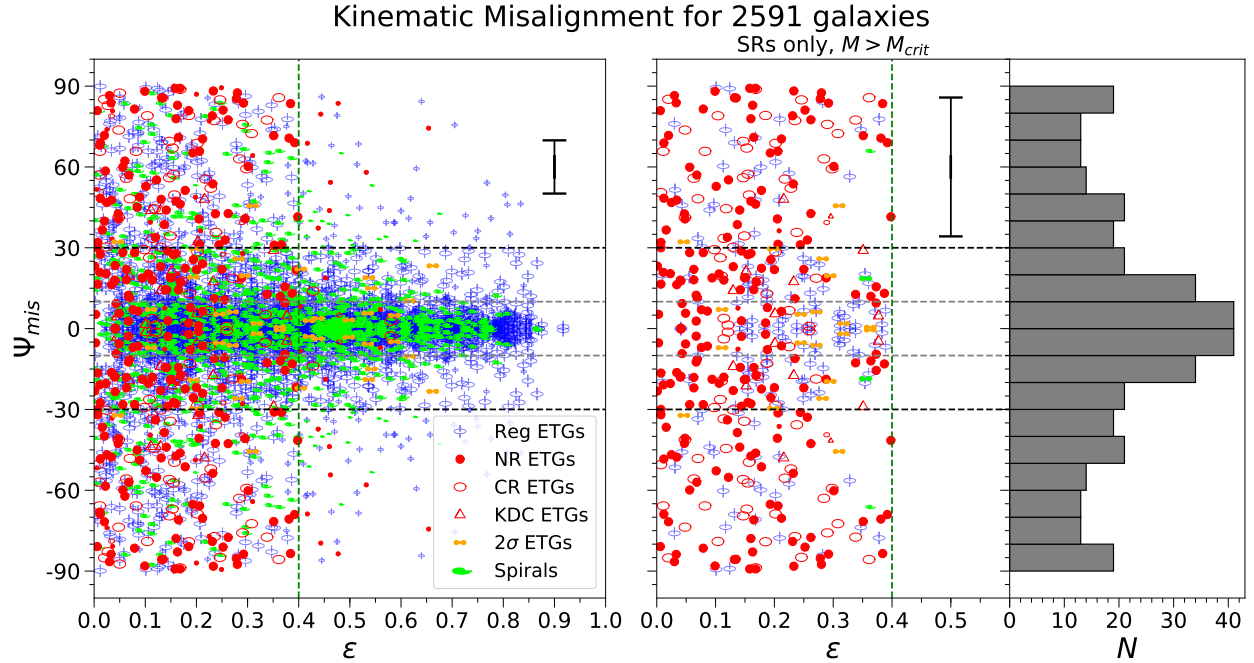


Fig. 6 Left panel: Misalignment (Ψ_{mis}) between the photometric axis (PA_{phot}) and kinematic axis (PA_{kin}) versus ellipticity (ϵ) for galaxies with classifiable kinematics (symbols as in Figure 4). Smaller symbols denote galaxies excluded from the clean sample. Each galaxy is symmetrically duplicated above and below the zero. The vertical dashed green line indicates the $\epsilon < 0.4$ criterion for slow rotators from Cappellari (2016, eq. 19). Black horizontal dashed lines mark the $|\Psi_{mis}| = 30^\circ$ and $|\Psi_{mis}| = 10^\circ$ thresholds. The typical error in PA is shown. Right panel: The same selection as the left panel, but only slow rotators with masses exceeding $M_{*}^{crit} = 2 \times 10^{11} M_{\odot}$ are displayed. A histogram of the distribution is included to the right of the scatter plot (Graham et al. 2018, fig. 12).

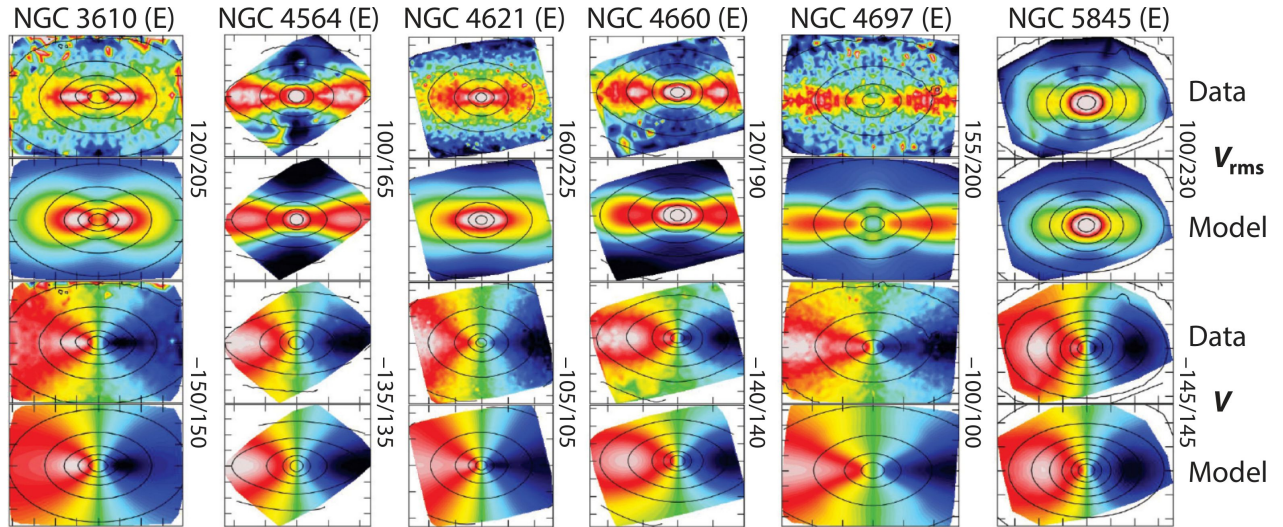


Fig. 7 Jeans Anisotropic Models with a cylindrically aligned velocity ellipsoid (JAM_{cyl}) applied to regular rotators morphologically classified as elliptical galaxies. Each plot is divided into four panels: Top: Symmetrized observed stellar $V_{rms} \equiv \sqrt{V^2 + \sigma^2}$. Second: Best-fitting JAM_{cyl} model for V_{rms} . Third: Symmetrized observed mean stellar velocity V . Bottom: Best fit to V using the optimal anisotropy β_z , inclination i , and mass-to-light ratio (M/L) derived from the V_{rms} fit, with only an overall scaling applied to V . These models accurately predict the shapes of both the V and V_{rms} stellar kinematics by adjusting only the anisotropy parameter β_z and choosing an inclination, underscoring the dynamical uniformity of regular rotators. Given that the total density in these models is proportional to the stellar density, the results also suggest that the total density slope closely approximates the stellar density within the fitted regions (Cappellari 2016, Fig. 10).

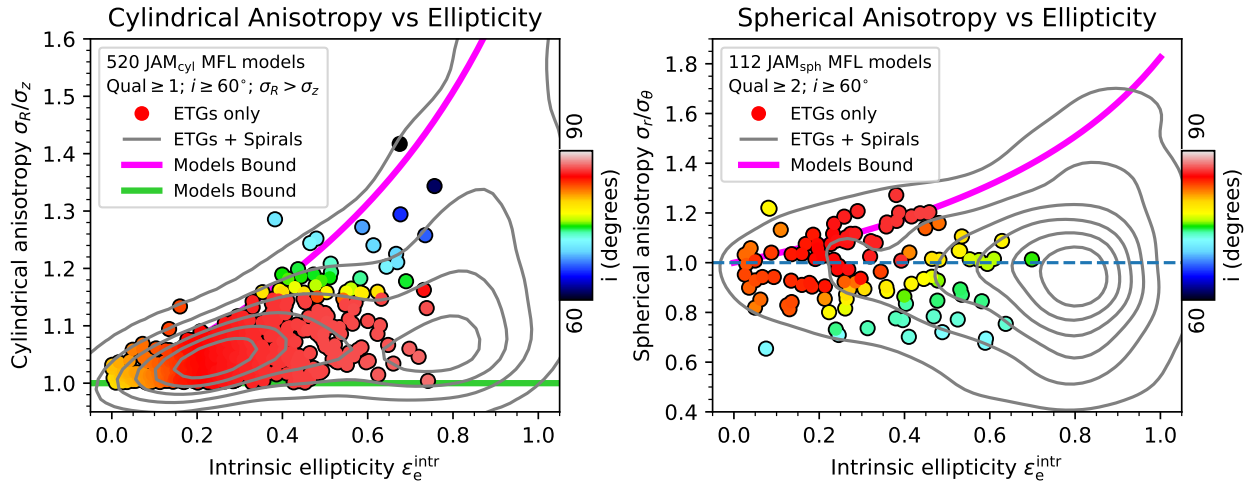


Fig. 8 Left panel: The mean anisotropy ratio σ_R/σ_z within the half-light radius ($R \lesssim R_e$) is shown for early-type galaxies (ETGs) from the MaNGA survey. These ETGs, classified morphologically as $T_{\text{type}} \leq -0.5$ by Vázquez-Mata et al. (2022), were analyzed using cylindrically-aligned Jeans Anisotropic Models (JAM_{cyl}) from Cappellari (2008). The sample includes galaxies with data quality $\text{Qual} \geq 1$ and inclinations $i > 60^\circ$ to minimize mass-deprojection and inclination-anisotropy degeneracies. The anisotropy ratio is plotted against the intrinsic ellipticity $\epsilon_e^{\text{intr}} \equiv 1 - \sqrt{1 + \epsilon_e(\epsilon_e - 2)/\sin^2 i}$, where ϵ_e is the observed ellipticity and i is the best-fitting model inclination. Similar results are obtained for $\text{Qual} \geq 2$, but the sample size is too small as I also exclude models on the lower boundary $\sigma_R = \sigma_z$ (green line). Right panel: The mean anisotropy ratio σ_r/σ_θ is shown for spherically-aligned models (JAM_{sph}) from Cappellari (2020), selected with $\text{Qual} \geq 2$. The models are constrained to approximately lie below the magenta line (and above the green line for the left panel). For this reason, the distribution of models between these lines should not be interpreted as an empirical trend. However, most models tend to avoid the magenta boundary, with a clear peak near the isotropy line (ratio = 1), especially when including spiral galaxies. Models closest to the magenta boundary, indicating high anisotropy, tend to have lower inclinations, suggesting their anisotropy may be overestimated due to mass-deprojection degeneracies. Gray contours represent a kernel density estimate of the number density for the general population, including both ETGs and spiral galaxies (using `scipy.stats.gaussian_kde`; Virtanen et al. 2020). Colors indicate the loess-smoothed mean inclination for ETGs only (using `loess.loess.2d`; Cappellari et al. 2013b). The anisotropy distribution of ETGs appears to smoothly extend that of spiral galaxies. These results are based on models where mass follows light (MFL) to reduce mass-anisotropy degeneracy. The total density is close to the true value within the regions ($R \lesssim R_e$) sampled by the kinematics. Similar, albeit noisier, results are obtained for models including an NFW halo. Data for this figure were taken from the DynPop catalog (Zhu et al. 2023, using the keywords `eps_mge`, `inc_deg`, `beta_z`, and `beta_r`). Note: The model bounds were determined using the intrinsic ellipticity derived from deprojected MGEs. This measure is not included in the catalog and, for galaxies with variable ellipticity, differs slightly from the ϵ_e^{intr} values displayed in the plots.

Made-to-Measure Technique: Introduced by Syer & Tremaine (1996). In its most general form, this technique tries to nudge a live non-steady-state N-body model towards fitting the observed kinematics. But no proof of convergence exists in this case. With a fixed gravitational potential it is conceptually similar to Schwarzschild’s approach, but less efficient.

The strength of Jeans’s method lies in its predictive power. One of its generalizations, the Jeans Anisotropic Modelling (JAM, Cappellari 2008, 2020) method has been applied to large samples of galaxies. It was found that, given the surface brightness distribution and assuming axisymmetry, the large variations in the kinematics of regular-rotator ETGs could be captured to good accuracy by just a couple of parameters: the inclination i and the global anisotropy, as illustrated in Figure 7. JAM was found to be more accurate in estimating galaxy densities than Schwarzschild’s technique for regular rotators, using both real data (Leung et al. 2018, fig. 8) and N-body simulations (Jin et al. 2019, fig. 4).

Anisotropy can be defined as the ratio between the velocity dispersion measured along different directions by a hypothetical observer in the galaxy moving with the average stellar velocity. It can be measured in different coordinate systems, such as cylindrical polar (R, ϕ, z) or spherical polar (r, θ, ϕ). In axisymmetry, the second velocity moments of the line-of-sight velocity $\overline{V_{\text{los}}^2}$ are independent of the anisotropy in the tangential (ϕ) direction. This is because one can always reverse the sense of rotation of galaxy stellar orbits without changing the gravitational potential or the orbital makeup while keeping $\overline{V_{\text{los}}^2}$ unchanged. Therefore, the key anisotropy parameters are: (i) in cylindrical coordinates, the ratio of the velocity dispersion in the axial and radial directions σ_z/σ_R , and (ii) in spherical coordinates, the ratio of the velocity dispersion in the angular and radial directions σ_θ/σ_r .

The global anisotropy distribution, extracted from the largest set of JAM dynamical models constructed so far (Zhu et al. 2023), is shown in Figure 8. For this figure, I selected a subset of galaxies with the best data and with fitted inclination $i > 60^\circ$ to reduce the effect of the light deprojection degeneracy. It shows that the anisotropy of ETGs strongly depends on ellipticity, with larger variations in anisotropy for intrinsically flatter galaxies, as first pointed out by Cappellari et al. (2007) and Thomas et al. (2009). However, in general, deviations from isotropy (i.e., equal dispersion in all coordinates) are rather small, typically $\lesssim 20\%$. Santucci et al. (2022) presented consistent results using Schwarzschild’s technique. However, the extra generality of the method, compared to JAM, results in much larger uncertainties and a

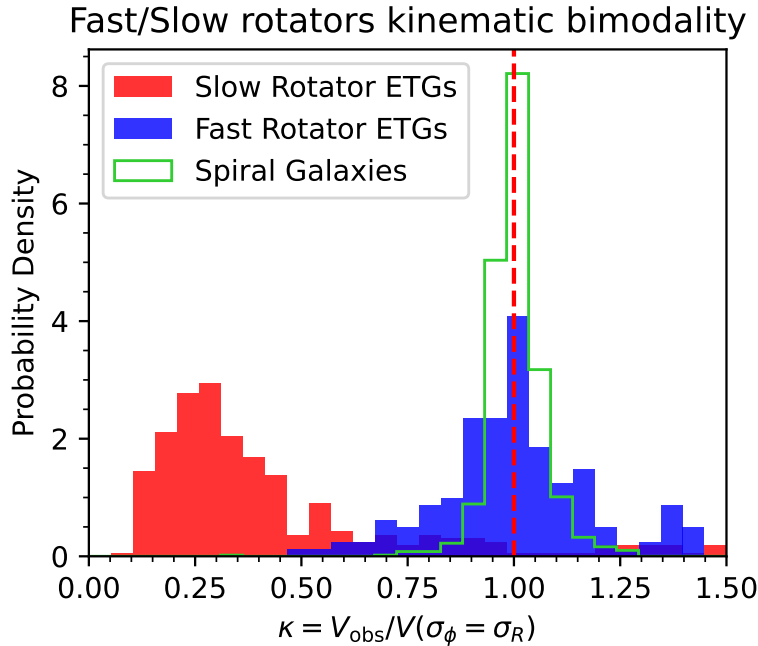


Fig. 9 Histogram of the ratio κ between the observed velocity V_{obs} and the velocity $V(\sigma_\phi = \sigma_R)$ predicted by a JAM_{cyl} mass-follows-light model with a cylindrically-aligned and oblate ($\sigma_R = \sigma_\phi \neq \sigma_z$) velocity ellipsoid. Similar results are obtained using JAM_{sph} models with a spherically-aligned velocity ellipsoid and $\sigma_r = \sigma_\phi \neq \sigma_\theta$. Specifically, κ is calculated as the ratio between the projected angular momenta of the data and the model (Cappellari 2008, eq. 52). The distribution peaks sharply around $\kappa = 1$, with an rms scatter that depends on data quality (see Zhu et al. 2023, fig. 10). Galaxies were selected with an inclination $i > 60^\circ$ to minimize mass-deprojection and inclination-anisotropy degeneracies. For fast rotators (classified via Equation (8)) and spiral galaxies (classified as $T_{\text{type}} > -0.5$ by Vázquez-Mata et al. 2022), a quality limit of $\text{Qual} \geq 3$ was applied, resulting in $N_{\text{fast}} = 160$ and $N_{\text{spiral}} = 961$ galaxies. For slow rotators, a lower quality threshold of $\text{Qual} \geq 1$ was adopted, yielding $N_{\text{gal}} = 489$ to improve statistics given their smaller fraction. All histograms represent probability densities, i.e., they are normalized to unit area. The fact that slow rotators exhibit less rotation than fast rotators is expected by design. However, the clear bimodality, the flat minimum between the two classes, and the clustering of fast rotators around $\kappa = 1$, similar to spiral galaxies, are not. This suggests that the two classes of ETGs are physically distinct and do not form a continuous distribution in angular momentum. The data for this figure were obtained from the DynPop catalog by Zhu et al. (2023, keyword kappa).

correspondingly larger scatter.

Figure 9 shows, for the same galaxy sample, the ratio $\kappa = V_{\text{obs}}/V(\sigma_\phi = \sigma_R)$ between the observed mean stellar velocity and the velocity of a JAM model with an oblate velocity ellipsoid ($\sigma_\phi = \sigma_R$). For regular rotator ETGs, this ratio is close to unity with high accuracy (see Cappellari 2016, fig. 11). This implies that, once the gravitational potential has been determined, by fitting the V_{rms} , the rotation of fast rotators can be predicted with high accuracy by assuming $\sigma_\phi = \sigma_R$. This further highlights the remarkable regularity of the kinematics of this class of galaxies.

Schwarzschild’s orbit-superposition method leverages the full information content of the line-of-sight velocity distribution (LOSVD) when high-quality kinematic data are available, enabling non-parametric recovery of the orbital structure. This approach has also been adapted to study stellar population properties (e.g., Poci et al. 2019). Radial anisotropy profiles derived for early-type galaxies (ETGs) with integral field spectroscopy (IFS) are shown in Figure 10, where σ_r denotes the radial velocity dispersion in spherical coordinates and $\sigma_{\text{tang}}^2 \equiv (\sigma_\theta^2 + \sigma_\phi^2)/2$ represents the azimuthally averaged tangential dispersion. These profiles typically transition from tangential anisotropy ($\sigma_{\text{tang}} > \sigma_r$) in the central regions to radial anisotropy ($\sigma_r > \sigma_{\text{tang}}$) at larger radii (Gebhardt et al. 2003; Cappellari et al. 2008; Thomas et al. 2014). Around R_e deviations from isotropy are generally mild ($\lesssim 20\%$). However, constraints on anisotropy at $r \gtrsim R_e$ remain unreliable due to degeneracies with dark halo modeling and sensitivity to systematic biases in low signal-to-noise data.

Thomas et al. (2014, fig. 2) performed a similar comparison between anisotropy profiles for core and core-less ETGs. Their result is qualitatively similar, with more homogeneous profiles for core galaxies than core-less ones. However, they find stronger anisotropy gradients for core galaxies. They attribute this to their inclusion of a dark-matter halo in their models. Dark matter makes the total density profile shallower, which in turn makes the anisotropy profile steeper, for fixed kinematics. Of the models in Figure 10, only the model for NGC 4486 includes a dark-matter halo. The other models assume the total density follows the light distribution, which is a good approximation for the regions sampled by kinematics (Figure 11). Although the inclusion of a dark halo would generally be preferable, there is degeneracy between anisotropy and the total density slope (Binney & Mamon 1982; Gerhard 1993). This could be lifted with high S/N integral-field kinematics allowing one to measure the full LOSVD. However, the large-scale data used by Thomas et al. (2014) are mostly based on sparse coverage and modest quality (Rusli et al. 2013). It is unclear whether they can reliably break the mass-anisotropy degeneracy. This is why I did not include these profiles in Figure 10. Models including a dark halo, but with data quality like the models of Figure 10 would be extremely valuable.

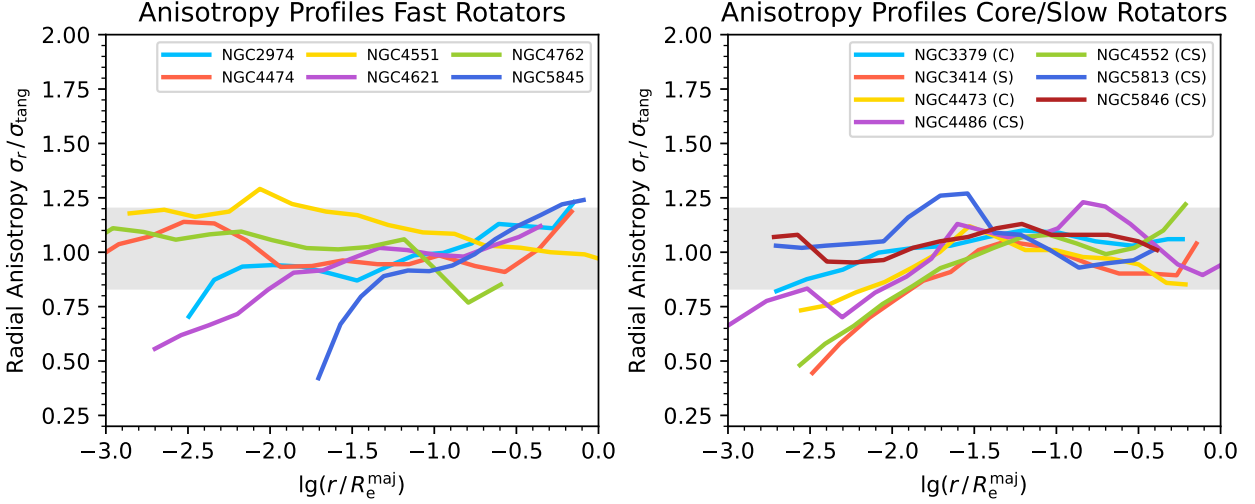


Fig. 10 Radial anisotropy profiles $\sigma_r/\sigma_{\text{tang}}$ obtained from a subset of Schwarzschild’s dynamical models, utilizing high-quality observational data. These profiles are derived from models that have been fitted to both high-resolution nuclear and large-scale ($\sim 1R_e$) high signal-to-noise (S/N) integral field stellar kinematics. In spherical coordinates, σ_r denotes the second moment of the velocity distribution along the radial direction, while $\sigma_{\text{tang}}^2 \equiv (\sigma_\theta^2 + \sigma_\phi^2)/2$ represents the average dispersion in the tangential directions. The anisotropy is defined in the standard way such that σ_{tang} excludes mean stellar rotation, and an isotropic system with $\sigma_r = \sigma_\theta = \sigma_\phi$ yields $\sigma_r/\sigma_{\text{tang}} = 1$, irrespective of rotation. Different lines correspond to measurements for distinct galaxies. A gray horizontal band indicates the reference range $5/6 < \sigma_r/\sigma_{\text{tang}} < 6/5$. The left panel displays models for fast rotators, while the right panel includes slow rotators (as defined by Equation (8), using $(\lambda_{R_e}, \varepsilon_e)$ from Emsellem et al. 2011) or galaxies with a nuclear core in their surface brightness profile (as per Krajnović et al. 2013). Parentheses next to galaxy names indicate core galaxies (C), slow rotators (S), or both (CS). Overall, the profiles in both panels are isotropic ($\sigma_r/\sigma_{\text{tang}} \approx 1$) within $\sim 20\%$ for $R_e/30 \lesssim r \lesssim R_e$. However, slow rotators and/or core galaxies exhibit a systematic trend toward tangential anisotropy within the core radius and near the central supermassive black hole ($r \lesssim R_e/100$). Fast rotators do not show a clear systematic trend in their nuclear anisotropy profiles. The uncertainties in the anisotropy profiles are dominated by systematic effects. The profiles are likely intrinsically smooth, implying that the observed $\sim 10\%$ fluctuations in individual profiles likely reflect statistical uncertainties. The anisotropy profile for NGC 3379 is sourced from Shapiro et al. (2006, fig. 15), while those for NGC 2974, NGC 3414, NGC 4473, NGC 4552, NGC 4621, NGC 5813, NGC 5845, and NGC 5846 are from Cappellari et al. (2008, fig. 2). The profile for NGC 4486 is from Gebhardt et al. (2011, fig. 7), and those for NGC 4474, NGC 4551, and NGC 4762 are from Krajnović et al. (2018, fig. 11).

3.4 Total Density Profiles and Dark Matter Distribution

The primary quantity that dynamical models can extract from kinematic data is the total density profile. Its robustness comes from the fact that the total density does not depend on assumptions about how to parametrize the luminous and dark matter components separately. In particular, this quantity is independent of possible gradients in the stellar population in galaxies.

Modeling the gravitational lensing of 58 ETGs revealed that, within the region $R \lesssim R_e/2$ constrained by the lenses, the density follows $\rho(r) \propto r^{-\gamma_{\text{tot}}}$ with (positive) logarithmic density slope $\gamma_{\text{tot}} \equiv -d \lg \rho(r)/d \lg r$ given by $\gamma_{\text{tot}} = 2.08 \pm 0.02$ (Koopmans et al. 2009; Auger et al. 2010). This is close to the isothermal slope $\gamma_{\text{tot}} = 2$, which corresponds to flat circular velocity curves. Dynamical models of the stellar kinematics of 14 regular-rotator ETGs, extending out to much larger radii of $\approx 4R_e$, found a slightly steeper slope $\gamma_{\text{tot}} = 2.19 \pm 0.03$ over the whole radial range, with equally small scatter (Cappellari et al. 2015).

This apparent ‘universal’ slope of the density profiles later turned out to be valid only for galaxies with large effective velocity dispersion σ_e . The slope is nearly constant, with little scatter, at $\gamma_{\text{tot}} \approx 2.2$ for $\lg(\sigma_e/\text{km s}^{-1}) \gtrsim 2.2$ but starts decreasing at lower σ_e (see fig. 22 of Cappellari 2016, and Poci et al. 2017). The trend is weak in ETGs, but becomes more apparent when including both spiral galaxies and ETGs, as the mean slopes for spirals reach $\gamma_{\text{tot}} \approx 1.5$ at $\lg(\sigma_e/\text{km s}^{-1}) \approx 1.7$ (Li et al. 2019; Zhu et al. 2024; Li et al. 2024). The left panel of Figure 11 shows the $\gamma_{\text{tot}} - \sigma_e$ relation for ETGs as a continuation of a smooth trend linking spirals and ETGs. The total slope γ_{tot} is lower for younger galaxies and tends to be systematically higher for ETGs, which have the oldest stellar populations (Zhu et al. 2024; Li et al. 2024).

To study the separate contributions of luminous and dark matter, which are key elements of our current galaxy-evolution paradigm, one must make additional assumptions: (i) adopt a parametrization, and possibly a shape, for the dark matter distribution; and (ii) decide how to extract and approximate the baryonic matter from observations.

The reliance on extra assumptions makes the results on dark matter distribution less robust than those on the total slopes. For example, if the dark matter profile approximates the stellar one and the total density is close to the stellar density, a change in the stellar M/L becomes indistinguishable from a change in the dark matter fraction $f_{\text{DM}}(R_e)$, using purely dynamical or strong gravitational lensing techniques. This situation frequently occurs in real ETGs, as the total slope is typically close to the stellar one (Cappellari et al. 2013a; Poci et al. 2017; Li et al. 2024; Figure 11).

The stellar mass distribution is inferred by deprojecting the observed surface brightness. This process is mathematically non-unique, even

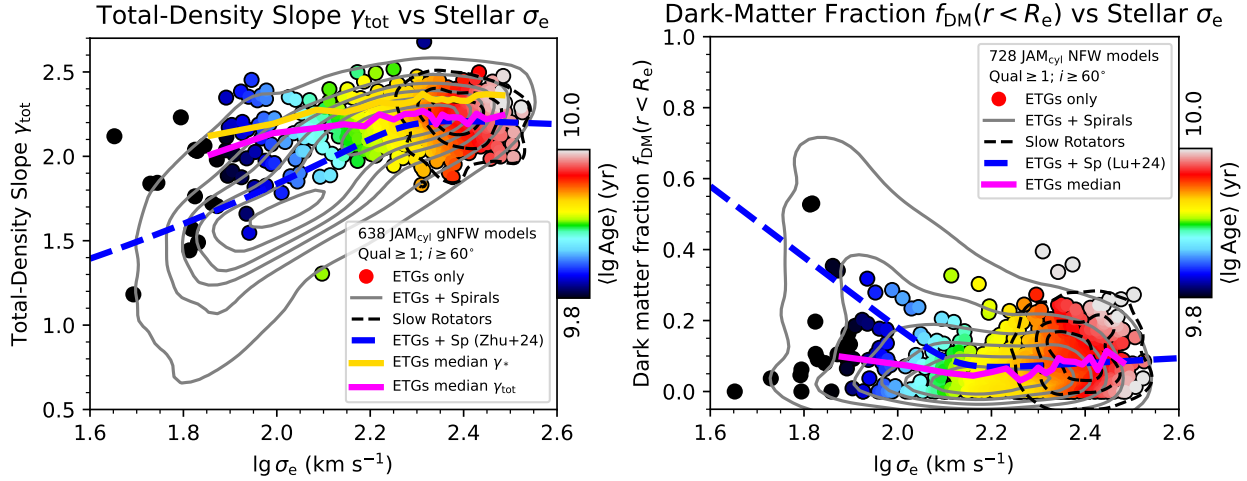


Fig. 11 Left panel: The mass-weighted total logarithmic density slopes γ_{tot} of Equation (5) within a sphere of radius $r = R_e$, as a function of galaxy effective velocity dispersion σ_e , for the most general JAM_{cyl} models with gNFW halo. The filled circles represent ETGs. They exhibit steeper total slopes at fixed σ_e compared to the overall galaxy population because they are generally older and follow the age-slope trend at fixed σ_e (Zhu et al. 2024, figs. 8 and 10). The blue dashed line is the best-fitting relation to the median of the whole population from Zhu et al. (2024, eq. 13). The gold solid line shows the median stellar luminosity density slope γ_* for the ETGs, computed in 20 bins of σ_e with an equal number of galaxies, and tracks γ_{tot} with a constant offset (Li et al. 2024, fig. 1). Right panel: The correlation between the dark matter fraction $f_{DM}(R_e)$ within a sphere of radius $1R_e$ and σ_e , from JAM_{cyl} models with an NFW halo. The blue dashed line represents the fit to the median values for the overall population, which remains nearly flat for $\lg(\sigma_e / \text{km s}^{-1}) \gtrsim 2.1$ and increases at lower σ_e (Lu et al. 2024, eq. 7). ETGs follow the overall trend at high σ_e but exhibit lower $f_{DM}(R_e)$ at lower σ_e , consistent with their steeper total density profiles in the left panel, primarily due to the steeper stellar density (larger bulge mass fraction) than spirals. The low $f_{DM}(R_e)$ for ETGs can also be inferred non-parametrically from Equation (6), using the values of γ_{tot} and γ_* in the left panel, assuming $\gamma_{DM} = 1$. In both panels, the filled circles represent ETGs (classified as $T_{type} \leq -0.5$ by Vázquez-Mata et al. 2022), colored by the loess-smoothed global luminosity-weighted age (using `loess.loess_2d`; Cappellari et al. 2013b). The magenta solid line indicates the median value for the ETGs alone, computed in 20 bins of σ_e with an equal number of galaxies. The gray contours show the kernel density estimate of the density distribution for the entire galaxy population of ETGs and spiral galaxies (using `scipy.stats.gaussian_kde`; Virtanen et al. 2020), while the black dashed contours is the same density for slow rotators alone. The data for this figure come from the DynPop catalog: the dynamical quantities from Zhu et al. (2023, keywords MW_Gt_Re, MW_Gs_Re, Sigma_Re), and the stellar ages from Lu et al. (2023, keyword LW_Age_Re).

if the galaxy is assumed axisymmetric with a known inclination, unless the galaxy is edge-on (Rybicki 1987; Gerhard & Binney 1996). The deprojection becomes much more degenerate for any viewing direction if the galaxy is assumed triaxial. This deprojection degeneracy is a major uncertainty in any dynamical modeling technique. Additionally, gradients in the stellar M/L , inferred from the galaxy’s stellar population or colors, must be included in the models, increasing the resulting uncertainties of the dark matter decomposition.

A common description for the dark matter distribution is the generalized Navarro, Frenk, and White (gNFW) profile (Wyithe et al. 2001):

$$\rho(r) = \rho_s \left(\frac{r_s}{r} \right)^\gamma \left(\frac{1}{2} + \frac{1}{2} \frac{r}{r_s} \right)^{\gamma-3}. \quad (4)$$

The density has the same large-radii asymptotic power-law slope $\rho(r) \propto r^{-3}$ as the NFW halo (Navarro et al. 1996), but it allows for a variable inner slope γ . The ranges include a flat inner core ($\gamma = 0$) and the NFW slope ($\gamma = 1$) as special cases. The gNFW profile is often used to describe the total density rather than just the dark matter.

Early studies on small samples of galaxies indicated that the dark matter fraction $f_{DM}(R_e)$ in ETGs contributes minimally to the total mass within $1R_e$ (e.g., Gerhard et al. 2001). A more extensive study involving 260 galaxies using IFS data and JAM models confirmed these findings, showing that the median $f_{DM}(R_e)$ was as low as 13% (Cappellari et al. 2013a). Recently, Lu et al. (2024) extended this analysis using JAM on a sample of over 2000 ETGs and more spirals. After carefully removing unreliable models, they reported a clear relationship between $f_{DM}(R_e)$ and σ_e , as shown in the right panel of Figure 11. Their median trend is flat for $\lg(\sigma_e / \text{km s}^{-1}) \gtrsim 2.1$ (close to where the $\gamma_{tot} - \sigma_e$ relation flattens), with $f_{DM}(R_e) \approx 9\%$.

Here, I repeated their analysis for the ETGs subsample alone. Following their methodology, I first used the $(M_*/L) - \sigma_e$ relation determined from JAM models to exclude likely unreliable models. For this, I employed the robust linear fitting method implemented in the `ltsfit` package⁴ described in Cappellari et al. (2013a), which combines the Least Trimmed Squares robust technique of Rousseeuw & Van Driessen (2006) with a least-squares fitting algorithm that accounts for errors in all variables, intrinsic scatter, and automatic outlier

⁴<https://pypi.org/project/ltsfit/>

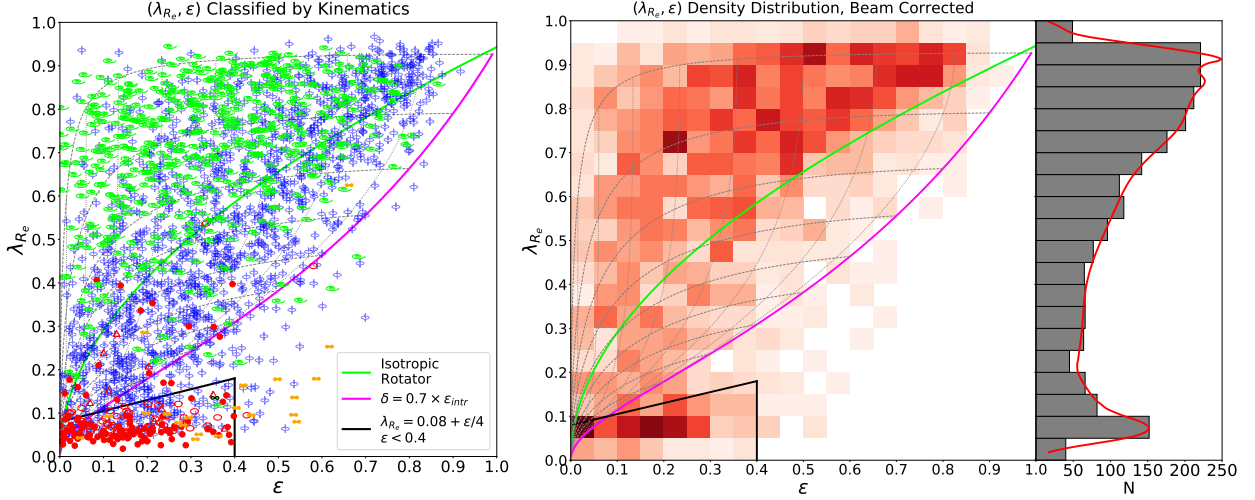


Fig. 12 Left panel: the $(\lambda_{R_e}, \epsilon_e)$ diagram is labeled according to kinematic morphology, with symbols representing ETGs as described in Figure 4, and spirals marked in green. The points represent the observed $(\lambda_{R_e}, \epsilon_e)$ values for 2,286 galaxies from the MaNGA survey, obtained through integral-field spectroscopy. The thick green line is the prediction for an edge-on ($i = 90^\circ$) isotropic rotator from Binney (2005), approximately converted from V/σ into λ_{R_e} (Emsellem et al. 2011, eq. B1), and the magenta line is the converted edge-on anisotropy-ellipticity relation $\delta = 0.7 \times \epsilon_e^{\text{intr}}$ from Cappellari et al. (2007). Thin dotted lines show the magenta line at different inclinations ($\Delta i = 10^\circ$), while black dashed lines trace how galaxies with a particular ϵ_e^{intr} at $i = 90^\circ$ move with changing inclination, using the formalism from Cappellari (2016, sec. 3.5, 3.6). The black trapezium in the lower-left corner define the region for slow rotator ETGs: $\lambda_{R_e} < 0.08 + \epsilon_e/4$, $\epsilon_e < 0.4$ (Cappellari 2016, eq. 19). Right panel: Same as in the left panel, but with the distribution of galaxies shown as a 2-dim histogram, and as a 1-dim histogram on the right. There is a clear peak in the galaxy distribution inside the trapezium defining the slow rotators (Graham et al. 2018, fig. 5).

detection.

I found that the relationship for ETGs is an extension of a trend including spirals, with ETGs showing systematically lower $f_{\text{DM}}(R_e)$ than spirals at a given σ_e . The dark matter density profiles show a preference for being steeper than the NFW slope ($\gamma = 1$) (Li et al. 2024), as predicted by the adiabatic contraction effect of baryons on dark matter particles during gas accretion (e.g., Gnedin et al. 2004). Broadly consistent results were presented by Santucci et al. (2022) using Schwarzschild’s method, though with much larger scatter due to the more flexible models, making it harder to detect any trend.

The trends in dark matter fraction can be understood without the need to assume any specific dark halo parametrization. When the logarithmic density slopes are mass-weighted, as shown in Figure 11, and defined by (Dutton & Treu 2014, eq. 1):

$$\langle \gamma(r) \rangle \equiv \frac{1}{M(r)} \int_0^r \gamma(x) 4\pi x^2 \rho(x) dx = \frac{1}{M(r)} \int_0^r -\frac{d \lg \rho(x)}{d \lg r} 4\pi x^2 \rho(x) dx = 3 - \frac{4\pi r^3 \rho(r)}{M(r)}, \quad (5)$$

there is a very simple yet rigorous relationship between the mass-weighted total slope γ_{tot} , dark halo slope γ_{DM} , stellar slope γ_* , and the dark matter fraction within the same radius. This relationship is independent of the assumed radial density profiles of the stars and dark matter:

$$f_{\text{DM}} = \frac{\gamma_{\text{tot}} - \gamma_*}{\gamma_{\text{DM}} - \gamma_*}. \quad (6)$$

It can be used to infer the dark matter fraction from the total and stellar slopes, which can be measured without degeneracies, while only assuming a mass-weighted dark-matter slope.

Assuming the mean dark-halo slope within $1R_e$ follows the NFW profile with $\gamma_{\text{DM}} = 1$, and adopting the nearly constant median offset $\gamma_* - \gamma_{\text{tot}} = 0.11$ that I measured for the ETG subsample (Figure 11 left), I derived from Equation (6) that f_{DM} ranges from 8% to 10% when γ_{tot} varies between 2.2 and 2.0. This simple estimate agrees with the detailed models shown in the right panel of Figure 11. One can also use Equation (6) to estimate the effect of possible halo contraction without running new models: For a maximally contracted dark halo with $\gamma_{\text{DM}} \approx 1.6$ (Cappellari et al. 2013a, fig. 2), the median dark matter fraction within R_e in ETGs would vary between 15% and 22%.

3.5 Quantitative Kinematic Classification

The results from the shape distribution in subsection 3.2 and dynamical modeling in subsection 3.3 demonstrate that ETGs are not a homogeneous class of objects. Instead, they can be separated into two distinct classes, showing a bimodal distribution in some key parameters:

Regular rotators: These galaxies show small kinematic misalignment and can be modeled as axisymmetric galaxies with stellar disks seen at various inclinations. They have homogeneous orbital makeup, display a range of anisotropies, and have highly predictable stellar rotation velocities or angular momenta.

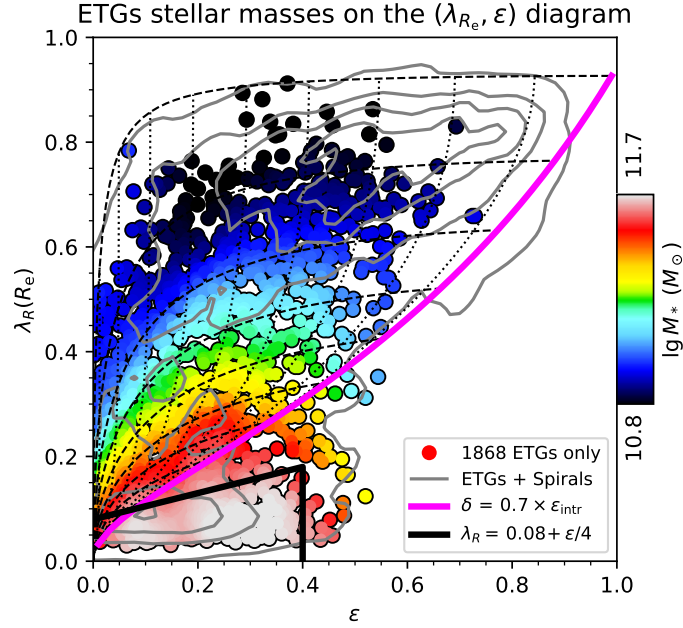


Fig. 13 Distribution of dynamically determined ETGs stellar masses on the $(\lambda_{R_e}, \epsilon_e)$ diagram. The masses are computed as $M_* \equiv (M/L)_{\text{JAM}} \times L$ using the JAM_{cyl} mass-follow-light models with $\text{Qual} \geq 1$, leading to a sample of $N_{\text{ETG}} = 1902$ ETGs. The magenta line represents the edge-on theoretical relation $\delta = 0.7 \times \epsilon_{\text{intr}}$ (Cappellari et al. 2007), which approximates the lower boundary of the region of the diagram enclosing most of the fast rotator and spiral galaxies. The dotted lines show how the relation transforms at different inclinations using equations from Cappellari (2016, sec. 3.5, 3.6). There are no ETGs flatter than $\epsilon_e \gtrsim 0.6$ as those tend to be morphologically misclassified as spirals, though flatter ETGs do exist (e.g., Figure 18). Contours of equal mass follow the dashed lines as predicted, indicating how galaxies of given intrinsic ellipticity ϵ_e^{intr} project at different inclinations. This projection is expected if ETGs of increasing mass have a characteristic ϵ_e^{intr} (due to a larger bulge) and are projected at random orientations. Massive ETGs tend to lie in the black trapezium of slow rotators (Cappellari 2016, eq. 19). The data for this figure come from the DynPop catalog by Zhu et al. (2023, keywords `Lambda_Re`, `Eps_MGE`, `Lum_tot_MGE`, `log_ML_dyn`). A version of this figure with both ETGs and spirals was shown in Lu et al. (2023, fig. 15). The filled disks represent ETGs, colored by the loess-smoothed global luminosity-weighted age (using `loess.loess_2d`; Cappellari et al. 2013b). The gray contours show the kernel density estimate of the density distribution for the entire galaxy population of ETGs and spiral galaxies (using `scipy.stats.gaussian.kde`; Virtanen et al. 2020).

Non-regular rotators: These galaxies are radically different. They are not axisymmetric but weakly triaxial and close to spherical, lacking stellar disks. Their rotation is generally negligible, except for possible kinematically-decoupled cores.

In two companion papers (Emsellem et al. 2007; Cappellari et al. 2007), the specific angular momentum parameter λ_R was introduced to separate these two kinematic classes using IFS kinematics in an (nearly) inclination-independent manner. This parameter provides a simple and reproducible way to classify galaxies:

$$\lambda_R \equiv \frac{\langle R|V| \rangle}{\langle R\sqrt{V^2 + \sigma^2} \rangle} = \frac{\sum_{n=1}^N F_n R_n |V_n|}{\sum_{n=1}^N F_n R_n \sqrt{V_n^2 + \sigma_n^2}}, \quad (7)$$

Here, F_n represents the fluxes within the N spatial bins where the mean stellar velocities V_n and velocity dispersions σ_n are measured. The summation extends to a specific finite radius R_{max} within a galaxy’s isophote. A common benchmark is to use $R_{\text{max}} = R_e$ and denote the parameter as λ_{R_e} .

The λ_R parameter is closely related to the V/σ rotation parameter (Binney 2005), which is instrumental in analyzing the interplay between shape, rotation, and anisotropy in ETGs. However, a significant distinction lies in the λ_R parameter’s sensitivity to the spatial distribution of velocities, unlike V/σ . Initially, the λ_R parameter was derived by substituting the velocity with the magnitude of the luminosity-weighted average projected angular momentum, expressed as $\langle \mathbf{L} \rangle = \langle \mathbf{R} \times \mathbf{V} \rangle$. To simplify computation and eliminate the need for determining vector directions, this was further simplified to $\langle R|V| \rangle$, producing equivalent results, where R represents the projected distance from the galaxy center. By making this proxy for angular momentum dimensionless and normalizing it with a quantity such as $V_{\text{rms}}^2 \equiv V^2 + \sigma^2$, which is proportional to the galaxy mass according to the scalar virial theorem (Binney & Tremaine 2008, sec. 4.8), the λ_R parameter is obtained (Emsellem et al. 2007).

Similar to the V/σ parameter, the λ_R kinematic proxy must be analyzed as a function of the galaxy’s apparent ellipticity (ϵ), both measured within the $1R_e$ isophote. The $(\lambda_{R_e}, \epsilon_e)$ diagram has been systematically applied to growing samples of early-type galaxies (ETGs): Emsellem et al. (2007) pioneered its use for 48 ETGs in the SAURON survey; Emsellem et al. (2011) extended it to 260 galaxies in ATLAS^{3D}; Falc3n-Barroso et al. (2019) to 600 galaxies in CALIFA; Graham et al. (2018) to 2,300 galaxies in MaNGA; and van de Sande et al. (2021a)

to 3,000 galaxies in SAMI. The largest application to date leverages the final MaNGA survey sample of 10,000 galaxies (Zhu et al. 2023), whose unprecedented size and data quality establish it as the current benchmark for global galaxy property studies. This work predominantly adopts MaNGA-derived figures due to its statistical robustness and kinematic quality.

Figure 12 shows the $(\lambda_{R_e}, \varepsilon_e)$ version by Graham et al. (2018), which includes the kinematic visual classification of Figure 4. The magenta line represents the edge-on theoretical anisotropy vs. ellipticity relation $\delta = 0.7 \times \varepsilon_e^{\text{intr}}$ (Cappellari et al. 2007), which approximately traces the lower envelope of the distribution of regular rotator ETGs (and spiral galaxies). This region contains disks with varying bulge fractions seen at random orientations. The bulge-free disks and spiral galaxies populate the top of the diagram, with more bulge-dominated systems having lower ε_e near the bottom of the magenta-line envelope. This lower envelope's existence can be attributed to an approximate limit to equilibrium solutions for the stellar orbits in galaxies with a nearly-oblate velocity ellipsoid (Wang et al. 2021). The black trapezium defines the new fast and slow rotator classification, quantitatively separating the two classes described at the beginning of this section. It is defined by (Cappellari 2016, eq. 19):

$$\lambda_{R_e} < 0.08 + \varepsilon_e/4 \quad \text{with} \quad \varepsilon_e < 0.4. \quad (8)$$

Most of the non-regular rotators visually classified with the scheme of Figure 4 fall within the slow-rotator region. Counterrotating disks can have λ_{R_e} values as low as slow rotators but are often significantly flatter. For $\varepsilon_e < 0.4$, the division in Equation (8) is very close to that by Emsellem et al. (2011), but it introduces a new limit in ellipticity to reduce the contamination of counterrotating disks, which are a physically distinct class of galaxies.

The middle panel of Figure 12 shows an approximate limit at $\lambda_{R_e} \approx 0.1$, separating fast and slow rotator ETGs naturally emerging from the data bimodality. The MaNGA sample used to construct the $(\lambda_{R_e}, \varepsilon_e)$ diagram was selected to be flat in stellar mass. However, a histogram of the λ_{R_e} values reveals a secondary peak within the slow-rotator trapezium region. A sharp transition in stellar masses is also observed between galaxies inside and outside the slow rotator trapezium. Figure 13 indicates that galaxies in the slow rotator box generally have larger masses than fast rotators of similar ε_e . Additionally, flat ($\varepsilon_e \geq 0.4$) galaxies below the magenta line have much smaller masses than slow rotators at lower ellipticity and are mainly spiral galaxies (see Lu et al. 2023, fig. 15, though not shown in Figure 13). This suggests that flat slowly rotating galaxies are distinct from the massive $M_* \gtrsim M_*^{\text{crit}} \approx 2 \times 10^{11} M_\odot$ slow rotator class. A statistical approach confirming bimodality in the (M_*, λ_{R_e}) plane is presented by van de Sande et al. (2021a, fig. 7).

The physical significance of the fast/slow rotator ETG bimodality is supported by the correlation between specific stellar angular momentum and the presence of cores in surface brightness profiles (subsection 2.3). Independent studies show overlap between slow rotators and cores in the central surface brightness (Lauer 2012; Krajnović et al. 2013).

The low mass of galaxies below the magenta line represents a significant empirical trend. A study of $M_* \approx 10^9 M_\odot$ galaxies in the MaNGA survey found that these low-mass galaxies, despite kinematic misalignment consistent with axisymmetry like more massive fast rotator ETGs, exhibit systematically lower specific angular momentum (Wang et al. 2024). However, as shown in Figure 15(e), their angular momentum is not as low as that of massive slow rotators with $M_* \gtrsim M_*^{\text{crit}}$. The low λ_{R_e} in these galaxies may be due to easier perturbation during their early gas-rich formation phase (e.g., Bland-Hawthorn et al. 2024) or the tendency of accreting gas disk spins to flip in less than an orbital time due to mergers and changes in cosmic-web streams at low masses (Dekel et al. 2020), leading to significant stellar counter-rotation in the remnant.

Having established the physical distinction between fast and slow rotator ETGs, it is instructive to compare this classification against Hubble's classic morphological classification. One finds that *just about 1/3 of galaxies morphologically classified as ellipticals are slow rotators* (Emsellem et al. 2011). This implies that Hubble's ellipticals classification is generally not physically meaningful, because in the vast majority of cases, it selects fast rotator ETGs. These are inclined galaxies with disks, which would be classified as either S0 or disky ellipticals if seen edge-on. This highlights the usefulness of using the new kinematic classification of ETGs.

4 Scaling Relations

4.1 Fundamental Plane and Mass Plane

When the first kinematic measurements became possible, it was found that elliptical galaxies follow a relation $L \propto \sigma^4$ between their total luminosity and stellar velocity dispersion (Faber & Jackson 1976). Shortly after, a relation was discovered between the galaxy's average surface brightness Σ_e inside $1R_e$ and their luminosity (Kormendy 1977).

To understand the meaning of these relations, one can use the virial theorem (Binney & Tremaine 2008, sec. 4.8; Courteau et al. 2014, sec. V). Galaxies may be expected to satisfy the virial equilibrium condition, which applies to isolated systems of particles moving under the influence of mutual gravity. For a distribution of stars in a steady state with spherical symmetry, the scalar virial relation is:

$$M = 3 \frac{r_g \langle v_{\text{LOS}}^2 \rangle_\infty}{G}, \quad (9)$$

where $\sigma_{\text{LOS}}^2 \equiv \langle v_{\text{LOS}}^2 \rangle_\infty$ is the line-of-sight second velocity moment integrated over all particles, $r_g \equiv 2M^2 / \int_0^\infty [M(r)/r]^2 dr$ is the gravitational radius of the particle distribution, and M is their total mass. The relation is *rigorously* insensitive to the anisotropy or orbital distribution of the stars. The radius r_g varies between 2.2 and 4.4 times the half-light radius R_e , for an assumed Sérsic projected mass distribution with $n = 1 - 10$ (Cappellari et al. 2013a, fig. 6).

A problem with Equation (9) is that the relevant quantities are not directly observable in real galaxies: (i) the kinematics can only be

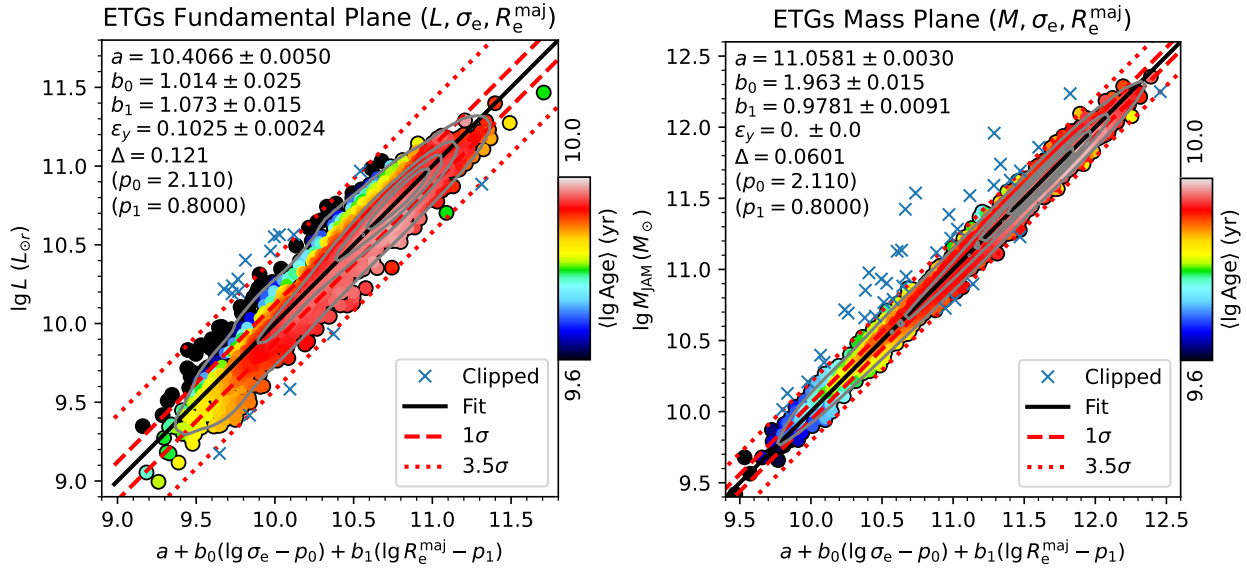


Fig. 14 Left panel: The Fundamental Plane of ETGs (classified as $T_{\text{type}} \leq -0.5$ by Vázquez-Mata et al. 2022) for the MaNGA sample, comprising $N_{\text{ETG}} = 1868$ ETGs with $\text{Qual} \geq 1$ from the DynPop sample of Zhu et al. (2023). The plane shows significant scatter, primarily due to a strong age dependency orthogonal to the plane. Right panel: The Mass Plane, obtained by transforming the luminosity from the left panel into masses as $M_{\text{JAM}} = (M/L)_{\text{JAM}} \times L$ using the mass-follow-light JAM_{cyt} dynamical models fitted to MaNGA stellar kinematics. The coefficients of the mass plane are close to the virial predictions $b_0 = 2$, $b_1 = 1$, and the observed rms scatter reduces from $\Delta = 0.12$ to $\Delta = 0.06$ dex, with intrinsic scatter consistent with zero, and any age trend orthogonal to the plane disappears. The fit was performed using the robust *lscfit* procedure by Cappellari et al. (2013a), and crosses represent the outliers automatically removed from the fit. The filled disks represent ETGs, colored by the loess-smoothed global luminosity-weighted age (using *loess.loess.2d*; Cappellari et al. 2013b). The gray contours show the kernel density estimate of the density distribution for the entire galaxy population of ETGs and spiral galaxies (using *scipy.stats.gaussian_kde*; Virtanen et al. 2020). This figure was adapted from Zhu et al. (2024, figs. 3, 4).

measured out to a finite radius and (ii) galaxies are thought to contain both luminous and dark matter, which means that M is not the mass of the visible stars from which we measure σ . This breaks the validity of the equation. For this reason, Equation (9) can only be used for studying qualitative trends and not for quantitative measurements. Nonetheless, the fact that the newly discovered Faber & Jackson (1976) relation did not follow the virial prediction was interpreted as indicating a smooth variation of the mass-to-light ratio M/L among galaxies.

A decade later, astrophysicists realized that the two previous relations are just special projections of a more general relation, aptly named the Fundamental Plane (FP, Dressler et al. 1987; Djorgovski & Davis 1987), between (L, σ_e, Σ_e) . Currently, one defines L as the galaxy’s total luminosity; R_e is the radius enclosing half of the total luminosity; and σ_e is the velocity dispersion integrated within a galaxy isophote of area πR_e^2 . Initially, astrophysicists used Σ_e as one of the three variables of the FP because both σ_e and Σ_e are distance-independent (ignoring cosmological surface-brightness dimming). This allows the FP to be used for measuring galaxy distances by scaling L to match a reference FP. However, $\Sigma_e = L/(2\pi R_e^2)$, which means that L appears in two of the FP coordinates, creating strong correlations. Nowadays, we think we know the geometry of our Universe quite accurately, and redshift is generally a more reliable distance indicator than the FP for distant galaxies (but see D’Eugenio et al. 2024b). To reduce the correlation between variables, a better form for the FP is $L \propto \sigma_e^b R_e^c$ (Cappellari et al. 2013a), which in logarithmic variables becomes the plane:

$$\lg L = a + b \lg \sigma_e + c \lg R_e. \quad (10)$$

If galaxies were self-similar stellar systems with the same M/L , then virial equilibrium would imply a relation $M \propto L \propto \sigma_e^2 R_e$. However, it was clear from the first determinations that the FP exponents are very different from the virial prediction $b = 2$, $c = 1$. Numerous determinations for different samples and with different techniques have confirmed this so-called ‘tilt’ of the FP over the past forty years (e.g., Colless et al. 2001; Bernardi et al. 2003; Cappellari et al. 2013a; D’Eugenio et al. 2021). As a recent example, the determination for the largest sample of ETGs of the MaNGA sample using high-quality IFS kinematics gives $b = 0.98 \pm 0.02$, $c = 1.03 \pm 0.02$ (Zhu et al. 2024).

After the discovery of the tilt, a rather long debate ensued (see review Cappellari 2016, sec. 4.1.2). This is because the tilt could be explained in several ways: (i) It could be a genuine variation in the M/L . This could be due to either changes in the stellar population ages or metallicity, or to changes in the dark matter fraction (subsection 3.4). (ii) Alternatively, the tilt could be due to non-homology, namely the fact that galaxies change structural properties as a function of their mass or velocity dispersion. In particular, we have seen that galaxies vary both their photometric profiles (subsection 2.2) and their kinematics (subsection 3.5) as a function of stellar mass.

One way to distinguish between the two alternatives is to directly measure the M/L of galaxies while modeling non-homology effects in detail. This can be done with either dynamical modeling (Cappellari 2016, sec. 3.4) or strong gravitational lensing (Treu et al. 2010) techniques. A first detailed study using Schwarzschild (1979) dynamical modeling of a sample of 25 galaxies concluded unambiguously that

the tilt of the FP was due almost entirely to a genuine M/L variation, and more specifically driven by a tight $(M/L) - \sigma_e$ relation, with homology having a negligible contribution (Cappellari et al. 2006). This result was later confirmed with samples of ever-increasing size and using the JAM method. The study of Cappellari et al. (2013a) modeled the 260 nearby ETGs of the ATLAS^{3D} sample; this was extended to about 2000 galaxies of all morphological types from the MaNGA sample by Li et al. (2018b), and to the full MaNGA galaxy sample of 10K galaxies by Zhu et al. (2024). The same conclusion was reached using 36 strong gravitational lens ETGs by Bolton et al. (2007) and 73 lens ETGs by Auger et al. (2010). All these studies transformed the FP into the Mass Plane (MP) by multiplying the luminosity by the total M/L within the central regions (typically $1R_e$). They consistently found that, unlike the FP, the MP essentially follows the Virial predictions. An illustration of this fact is shown in Figure 14 from the currently largest MaNGA detailed dynamical modeling study by Zhu et al. (2024). Importantly, the precise coefficients of the FP and MP were found to depend sensitively on how the parameters (M , σ_e , R_e) are measured (see the papers for details).

Given the rather small fraction of dark matter in the central region of ETGs (Cappellari et al. 2013a; Santucci et al. 2022; Zhu et al. 2024; Figure 11 right), the M/L variation must be almost entirely driven by variations in the stellar population (Graves et al. 2009; Falc3n-Barroso et al. 2011; Magoulas et al. 2012; D’Eugenio et al. 2021), including variations in the stellar initial mass function (van Dokkum & Conroy 2010; Cappellari et al. 2012, 2013b; Spiniello et al. 2012). Given that nearly all M/L variation happens as a function of the stellar velocity dispersion, as I will discuss in subsection 4.3, the tilt of the FP can be accurately predicted by the $(M/L) - \sigma_e$ relation alone (Cappellari 2016, sec. 4.2).

4.2 The Virial Mass Estimator

For maximum accuracy in determining the dynamical masses of galaxies, one should use dynamical models like JAM or Schwarzschild’s method. JAM is more accurate when only V and σ can be reliably measured from the single-aperture of integral-field data. Schwarzschild’s method can exploit the highest-quality integral-field kinematics, fitting the higher-order moments of the LOSVD. Both models require minimal assumptions and can model the instrumental PSF, the size of the observed aperture, or fit two-dimensional kinematics in detail. Nonetheless, the virial estimator has been used in numerous papers and holds historical significance. It is still used today in some cases.

The mass of a galaxy is generally an ill-defined concept from an empirical standpoint. Galaxies are extended objects with fuzzy boundaries, consisting of stars in the central regions and extended dark halos further out. Except for very rare situations, there are no tracers, either from dynamics or gravitational lensing, that can sample the full extent of an individual galaxy and allow us to measure its total mass. Only weak gravitational lensing can come close to measuring the galaxy’s total mass, but this is done in an assumption-dependent statistical manner, rather than for individual objects (see review by Mandelbaum 2018). Instead, the quantity that both dynamical models and strong gravitational lensing directly measure is the density profile within the region covered by the tracer (the FoV of the kinematic observations, or the Einstein radius of the lens, which is generally $< R_e$). The variation in density is dominated by variations in surface brightness, which varies by many orders of magnitude within a galaxy and is therefore not very meaningful. Much more meaningful is the M/L within the region covered by the tracer, which generally varies spatially by less than a factor of 1.5.

Two common ways to measure the virial parameters (L , R_e) are: (i) by fitting S3ersic profiles to the galaxy images, or (ii) essentially non-parametrically, using the Multi-Gaussian Expansion (Emsellem et al. 1994; Cappellari 2002). Using S3ersic profiles is especially common at high redshift (e.g., van der Wel et al. 2014), where the spatial resolution is limited, and the S3ersic profile captures most of the information in the data, while MGE is often used with well-resolved photometry (e.g., Cappellari et al. 2013a). The S3ersic profile is also useful to study correlations with other galaxy properties (e.g., Figure 2).

In either case, one can construct a version of the scalar virial relation from Equation (9) for quantitative determinations as follows: (i) measure the well-defined total M/L within a given spherical radius r_M , instead of the poorly-defined total mass; (ii) measure the luminosity-weighted σ_{LOS} within a finite aperture R_σ . A common choice of radii is $r_M = R_\sigma = R_e$, in which case $\sigma_e^2 \equiv \langle v_{\text{LOS}}^2 \rangle_{R_e}$ and the virial relation becomes:

$$(M/L)(r < R_e) \approx k_{\text{vir}} \frac{R_e \sigma_e^2}{GL}, \quad (11)$$

where k_{vir} is a coefficient calibrated using dynamical models. It was found that k_{vir} crucially depends on how the virial parameters are measured (Cappellari et al. 2013a, fig. 14), as well as on the galaxies’ inclination (van der Wel et al. 2022):

MGEs: When (R_e , L) are measured using MGEs, which do not involve extrapolating the galaxy luminosity L to infinite radii, the coefficient k_{vir} is nearly constant around $k_{\text{vir}} = 4 - 5$ (Cappellari et al. 2006). However, the precise value of k_{vir} depends on the depth of the observed photometry, making this method ideal for obtaining accurate scaling relation with homogeneous data, but generally unreliable for accurate absolute M/L determinations;

S3ersic: When (R_e , L) are measured by fitting S3ersic photometric models, and L represents the total galaxy luminosity extrapolated to infinite radii, then $k_{\text{vir}}(n)$ is a strong function of the S3ersic index. The functional form of k_{vir} can be predicted using models in absolute terms. However, this method relies on the assumption that galaxies under study are accurately described by the S3ersic profile, which is generally a crude approximation.

A common expression for $k_{\text{vir}}(n)$ can be found in Cappellari et al. (2006, eq. 20). However, this expression was computed for the interval $n = [2, 10]$. As such, it misses the maximum of $k_{\text{vir}}(n)$ at $n \approx 1.1$ and becomes significantly inaccurate for smaller values of n (e.g., 19% error at $n = 0.5$), which are typical in spiral galaxies (see Figure 2, right panel). To address this, I utilized the `jam.sph.proj` function within

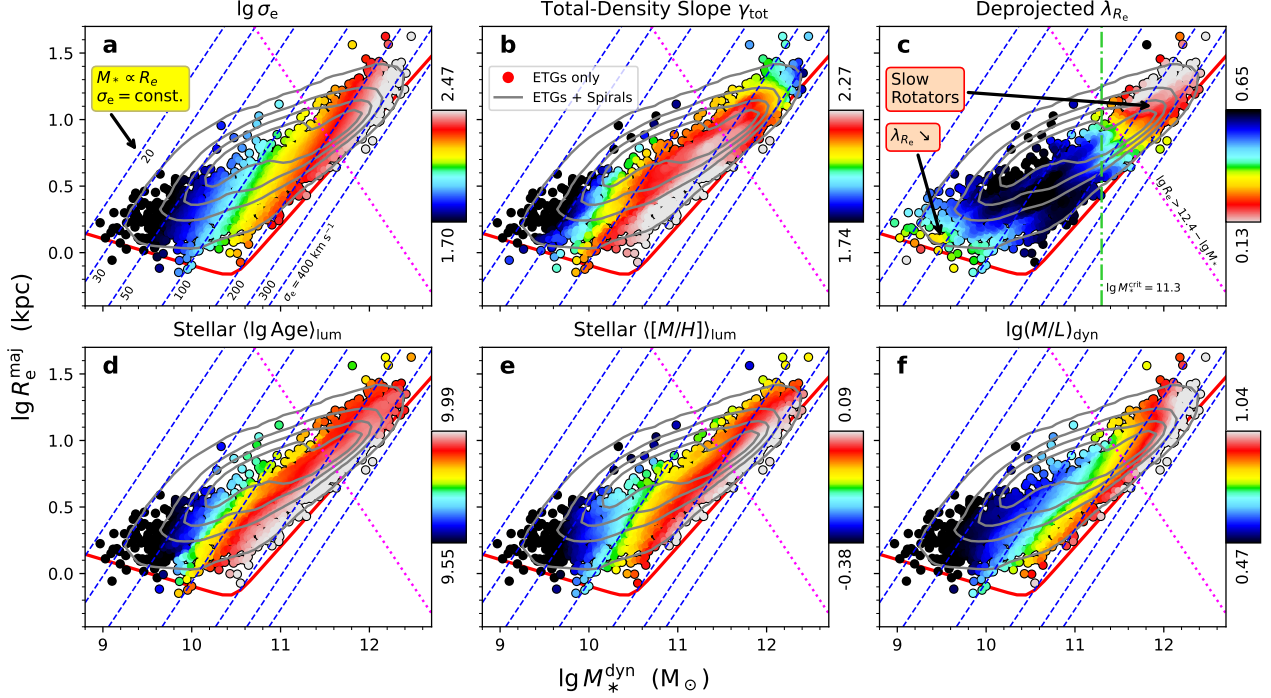


Fig. 15 Distributions of global physical properties of 2729 early-type galaxies (ETGs) on the stellar mass–effective radius (M_* , R_e^{maj}) plane, displaying six parameters: (a) effective luminosity-weighted velocity dispersion $\sigma_e^2 \equiv \langle V^2 + \sigma^2 \rangle$ within the half-light radius R_e ; (b) mass-weighted total density slope (see Equation (5)) from cylindrically-aligned JAM_{cyl} models with NFW dark halos; (c) deprojected intrinsic specific angular momentum $\lambda_{R_e}^{\text{intr}} = \lambda_{R_e} / \sin i$, edge-on corrected using JAM_{cyl} -derived inclinations i ; (d) luminosity-weighted stellar age; (e) luminosity-weighted metallicity; and (f) total dynamical mass-to-light ratio M/L from mass-follows-light JAM_{cyl} models. Distributions are smoothed via the LOESS algorithm (`loess.loess_2d`; Cappellari et al. 2013b) with `frac = 0.1`. Dashed curves trace lines of constant effective velocity dispersion σ_e from the scalar virial relation $\sigma_e^2 \equiv GM_{\text{JAM}} / (5R_e^{\text{maj}})$ (factor 5 from Cappellari et al. 2006). The red solid curve marks the zone of exclusion (ZOE) from Cappellari et al. (2013b), while grey contours show the kernel density estimate of galaxy density (including ETGs and spirals) using `scipy.stats.gaussian_kde` (Virtanen et al. 2020). In all panels, excluding (c), trends follow constant- σ_e lines (i.e., $M_* \propto R_e$), below the high-mass slow-rotator boundary defined by the magenta dotted line $\lg(R_e/\text{kpc}) \geq 12.4 - \lg(M_*/M_\odot)$. Panel (d) diverges: trends align orthogonally to constant- σ_e lines. Massive slow rotators dominate above $\lg(M_*^{\text{crit}}/M_\odot) \geq 11.3$ (or more precisely above the dotted magenta boundary), while a distinct low-mass population of slow-rotating galaxies (arrow-indicated) emerges below $\lg(M_*/M_\odot) \leq 9.5$, though their rotation is less suppressed compared to the extreme slow rotation of their massive counterparts. Parameters are sourced from the MaNGA DynPop catalog: dynamical quantities (catalog keywords `Sigma_Re`, `MW_Gt_Re`, `Lambda_Re`, `log_ML_dyn`, `Lum_tot_MGE`, `Rmaj_kpc_MGE`) from Zhu et al. (2023), and stellar population properties (catalog keywords `LW_Age_Re`, `LW_Metal_Re`) from Lu et al. (2023). Panels (a)–(c) were originally presented for the combined spiral and ETG sample in Zhu et al. (2024, fig. 16), while panels (d)–(f) in Lu et al. (2023, fig. 8).

the JAM package⁵ to compute the virial coefficient for various $\lg n$ values. This computation assumed the same spherical isotropic condition and integrated within an aperture of radius $R = R_e$ as done by Cappellari et al. (2006). I then derived a rational-function approximation for $k_{\text{vir}}(n)$, with a maximum relative error of 0.4% over an extended interval $n = [0.5, 16]$.

$$\lg k_{\text{vir}}(n) = \frac{0.8794 - 0.3405 \lg n - 0.2636 (\lg n)^2}{1 - 0.4194 \lg n}. \quad (12)$$

In the interval $n = [2, 10]$ this function agrees within 0.5% with the previous one as expected.

4.3 The Mass Versus Size Distribution

In subsection 4.1, I showed that the existence of the Fundamental Plane and Mass Plane are almost entirely due to virial equilibrium combined with a smooth variation of the galaxies’ stellar population and M/L . Virial equilibrium applies to any isolated system, regardless of how it reached that equilibrium, implying limited information on galaxy evolution is encoded in those relations.

When we look at the FP or MP far from an edge-on view, we see that galaxies are not distributed randomly on that plane. Given the thinness of the MP, the perspective does not significantly affect the plane’s appearance, provided we are not too close to an edge-on view. A particularly useful view of the MP is the (M, R_e) distribution (Figure 15), as both mass and size are quantities that are easy to measure and

⁵<https://pypi.org/project/jampy/>

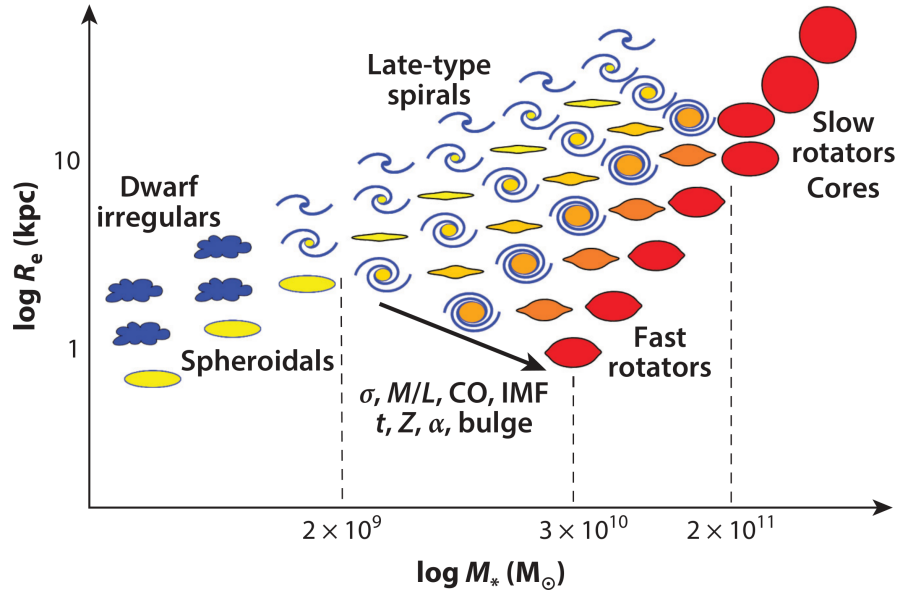


Fig. 16 Schematic distribution of galaxy properties on the stellar mass (M_*) vs. half-light radius (R_e) plane. Early-type galaxy (ETG) characteristics—such as stellar population parameters (ages, metallicity, α -enhancement, IMF) and gas content (CO mass fraction)—correlate along lines of nearly constant effective velocity dispersion σ_e (equivalent to $R_e \propto M_*$), tracing the bulge mass fraction or the steepness of the total mass density profile (γ_{tot}). This sequence transitions smoothly into the spiral galaxy population: minimal overlap occurs between late-type spirals (Sc-Irr) and ETGs, significant overlap exists between early-type spirals (Sa-Sb) and low mass-to-light ratio (M/L) fast rotators, and no overlap is seen between spirals and high- M/L fast rotators. Three key mass scales define distinct regimes: (i) $M_* \lesssim 2 \times 10^9 M_\odot$: Regular ETGs are absent, and the lower boundary of the mass-size relation rises with increasing mass. (ii) $M_* \approx 3 \times 10^{10} M_\odot$: ETGs reach minimum sizes (or maximum stellar densities), with the slope of the mass-size lower boundary steepening to $R_e \propto M^{0.75}$ at higher masses. (iii) $M_* \lesssim 2 \times 10^{11} M_\odot$: ETGs are dominated by flat fast rotators with disks. Above this threshold, spirals become rare, and the population transitions to round/weakly triaxial slow rotators with flat (core/deficit) central surface brightness profiles. (adapted from Cappellari et al. 2013b, fig. 14)

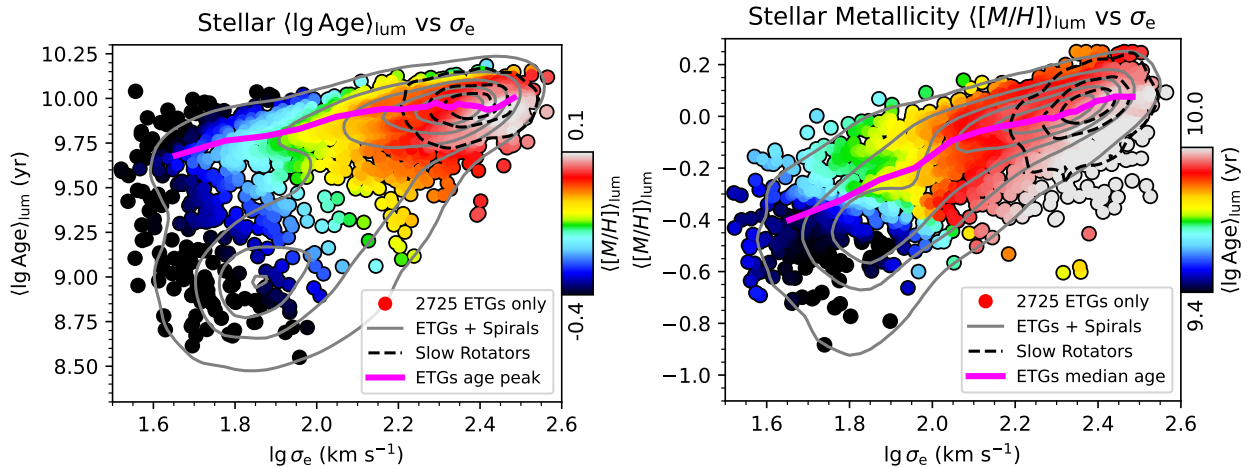


Fig. 17 Left panel: Distribution of global luminosity-weighted mean age $\langle \text{lg Age} \rangle_{\text{lum}}$ within the effective radius R_e versus effective velocity dispersion σ_e for early-type galaxies (ETGs; $T_{\text{type}} \leq -0.5$; Vázquez-Mata et al. 2022). Symbols are colored by the LOESS-smoothed global luminosity-weighted metallicity $\langle [M/H] \rangle_{\text{lum}}$ within R_e (via `loess.loess_2d`; Cappellari et al. 2013b). The magenta solid line traces the mode of the age distribution at fixed σ_e , calculated in 20 equal-number σ_e bins by identifying the peak of a kernel density estimate (KDE) in each bin. This method emphasizes the narrow ridge in the asymmetric age distribution. Right panel: Distribution of global luminosity-weighted metallicity $\langle [M/H] \rangle_{\text{lum}}$ versus σ_e , colored by $\langle \text{lg Age} \rangle_{\text{lum}}$; the magenta line shows the median metallicity in σ_e bins. In both panels, gray contours represent the KDE of the density distribution for all ETGs and spiral galaxies (using `scipy.stats.gaussian_kde`; Virtanen et al. 2020), while black dashed contours correspond to slow rotators. Data are from the MaNGA DynPop catalog: σ_e values (`Sigma_Re`) from Zhu et al. (2023), and stellar ages/metallicities (`LW_Age_Re`, `LW_Meta1_Re`) from Lu et al. (2023). A combined version (ETGs + spirals) appears in Lu et al. (2023, Fig. 6).

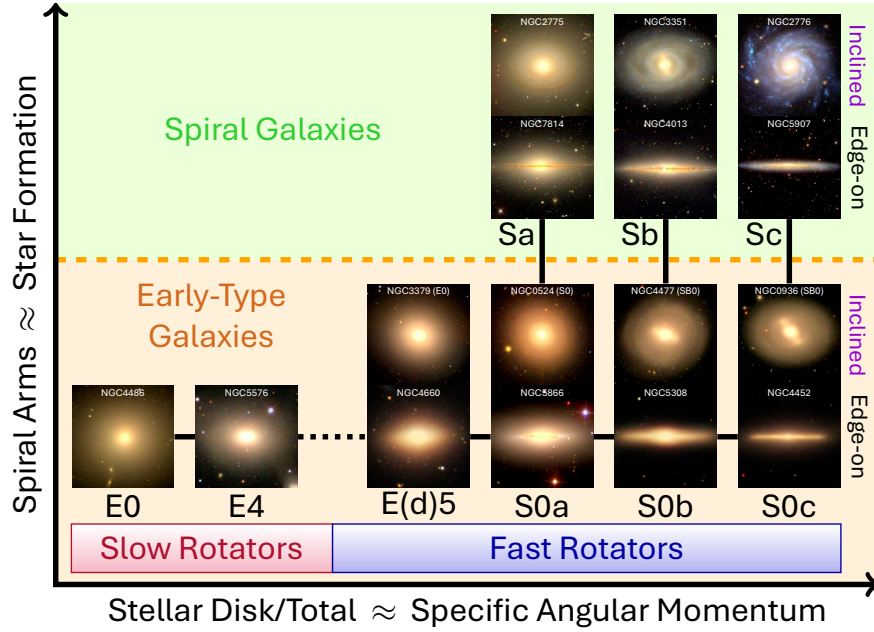


Fig. 18 This ‘comb’ diagram maps the systematic relationships between morphological features (e.g., disk-to-total stellar mass fraction, spiral arm prominence) and stellar kinematic properties (e.g., angular momentum, rotation curves) of galaxies. The x-axis quantifies the disk-to-total mass ratio (D/T), which correlates with specific stellar angular momentum λ_{R_e} within the half-light radius R_e and disk spatial extent, while the y-axis reflects spiral arm strength, tied to star formation activity or stellar population age. Fast-rotator early-type galaxies (ETGs), when edge-on, resemble S0s or disky ellipticals (E(d), Kormendy & Bender 1996), while many show bars when at low inclination (e.g., NGC 4477 or NGC 0936), or dusty disks (e.g., NGC 0524 or NGC 5866), yet photometry alone often misclassifies them: $\sim 2/3$ of morphologically labeled ellipticals (e.g., NGC 3379) are fast rotators. These systems span the full D/T range: from spheroid-dominated galaxies with compact stellar disks confined to $\lesssim R_e$ (e.g., NGC 4660, where the spheroid dominates at large radii) to galaxies dominated by thin, extended stellar disks prominent at large radii (e.g., NGC 4452). Kinematically, spheroid-dominated fast rotators display a stellar mean rotation curve that peaks within R_e and declines beyond it (Cappellari 2016, fig. 3a), while galaxies with higher disk-to-total mass ratios (D/T) exhibit rotation peaks at larger radii (Cappellari 2016, fig. 3b) or reduced σ_e at fixed stellar mass. Slow rotators are intrinsically round ($\varepsilon_e^{\text{intr}} \lesssim 0.4$) and always appear so in projection. Dynamical models and statistical inversion confirm fast rotators are flatter ($\varepsilon_e^{\text{intr}} \gtrsim 0.4$) than slow rotators. Solid lines denote empirical continuity; dashed lines mark the fast/slow rotator bimodality (Cappellari et al. 2011b, fig. 1). Flat ETGs are rare compared to flat spirals; diagram proportions do not reflect galaxy abundances.

nearly uncorrelated observationally. Moreover, galaxy masses and sizes are expected to vary in a clear and qualitatively predictable way during galaxy evolution. For this reason, the (M, R_e) distribution represents one of the cleanest benchmarks against which to compare galaxy evolution models.

Here, the mass $M = M_*^{\text{dyn}}$ represents the most accurate estimator of the total stellar mass M_* (see Cappellari et al. 2013a). This is because dark matter is generally negligible in ETGs. Thus, the dynamical $(M/L)(r < R_e)$ approximates the stellar population $(M_*/L)_{\text{pop}}$, implying that $(M/L)(r < R_e) \times L \approx (M_*/L)_{\text{pop}} \times L \approx M_*$.

The clearest and most striking feature of Figure 15 is that neither the galaxies’ stellar mass nor sizes are the main drivers of galaxy properties. Instead, both the parameters related to galaxy dynamics, such as M/L and dark matter fraction f_{DM} , and parameters describing the stellar population, such as age and metallicity, are nearly constant along lines with $M_* \propto R_e$, which correspond to lines of constant velocity dispersion $\sigma_e \propto \sqrt{M_*/R_e}$ according to the virial estimator.

Only the deprojected stellar specific angular momentum λ_{R_e} behaves differently. Below $M_*^{\text{crit}} \approx 2 \times 10^{11} M_\odot$, there is no trends with σ_e . Nearly all ETGs in this low-mass regime have the large λ_{R_e} characteristic of fast rotators. These ETGs are a population of randomly inclined, nearly axisymmetric galaxies with stellar disks. However, above M_*^{crit} there is a sharp transition to much lower λ_{R_e} (Emsellem et al. 2011; Cappellari et al. 2013b; Veale et al. 2017; Graham et al. 2018). This is the M_* regime where slow rotators start appearing in the ETG population (see review in Cappellari 2016). Panel (c) of Figure 15 reveals that and even better fast/slow rotator ETGs separation can be achieving by using a line orthogonal (i.e., with $R_e \propto -M_*$) to lines of constant σ_e (i.e., with $R_e \propto M_*$) and with stellar mass above M_*^{crit}

$$\lg(R_e/\text{kpc}) \gtrsim 12.4 - \lg(M_*/M_\odot). \quad (13)$$

Below the limit defined by Equation (13) the trend in ETGs merges smoothly with that of spiral galaxies, which occupy the region of low σ_e in the (M, R_e) plane (Cappellari et al. 2013b). The population and dynamical properties of spiral galaxies also follow the same constant- σ_e distribution as ETGs (Li et al. 2018b; Lu et al. 2023). This parallelism is crucial for understanding ETG evolution. A similar

parallelism between spiral galaxies and fast rotator ETGs can be observed when studying the star formation rate versus stellar mass $SFR - M_*$ relation (e.g., Brinchmann et al. 2004; Noeske et al. 2007). Below M_*^{crit} , fast rotator ETGs lie as expected below the star-forming main sequence, which is populated by spiral galaxies, but show only a small increase in their specific angular momentum. This is due to their more massive bulges, compared to spiral galaxies of similar mass. In contrast, above M_*^{crit} , in the region where slow rotators start dominating the ETGs population, a decrease in SFR is accompanied by a sharp decrease in λ_{R_e} (Wang et al. 2020; Cortese et al. 2022).

As seen from Equation (9), when the ratio of M to R_e is constant, the integrated second velocity moment σ_{LOS}^2 is expected to be nearly constant as well. Empirically, using masses from detailed dynamical models, it was found that the virial formula $\sigma_e^2 = GM/(k_{\text{vir}}R_e)$ accurately predicts the corresponding observable stellar σ_e (Cappellari et al. 2013a). The fact that galaxy properties follow lines with $M \propto R_e$ indicates that the stellar velocity dispersion σ_e , or a virial estimate based on masses and sizes, better predicts galaxy properties than masses M , radii R_e , or effective surface density Σ_e . This correlation was initially pointed out from a small galaxy sample with dynamical models in the SAURON survey (Cappellari et al. 2006). It was confirmed and generalized to other stellar population parameters with dynamical models of ever-increasing samples of galaxies from the ATLAS^{3D} (Cappellari et al. 2013b; McDermid et al. 2015), SAMI (Scott et al. 2017; Barone et al. 2018), and MaNGA surveys (Li et al. 2018b; Zhu et al. 2024). Similar results were also found using the virial estimator alone in the SDSS survey (Graves et al. 2009) and using photometry alone (Franx et al. 2008; Bell et al. 2012).

A similarly good predictor of galaxy properties is the core density Σ_1 , measured within a fixed aperture of $R = 1$ pc, which is generally smaller than R_e and samples the central region of galaxies (Cheung et al. 2012; Barro et al. 2017). In some of the discussions that follow, I will focus on σ_e , but the same conclusions apply if one replaces the stellar velocity dispersion σ_e with its virial estimate $\sigma_e \propto \sqrt{M/R_e}$ or the core density Σ_1 . The similarity between Σ_1 and σ_e is illustrated in Fang et al. (2013) and Cappellari (2023). The relation between galaxy properties and σ_e , leading to parallel sequences of equal σ_e , or equivalently $M_* \propto R_e$, on the (M_*, R_e) diagram, was highlighted in the review by Cappellari (2016, fig. 23), and I reproduce it here in Figure 16.

The dependence of galaxy properties on σ_e has important implications for understanding galaxy formation. At fixed stellar mass, both the velocity dispersion σ_e and the core density Σ_1 quantify the concentration of stellar mass near the center, or the prominence of the stellar bulge or spheroid. The σ_e is also the empirical quantity most tightly correlated with the mass of the central supermassive black hole (SMBH) (see review by Kormendy & Ho 2013). The empirical correlation tells us that when galaxies quench their star formation and become passive and metal-rich ETGs, they also grow their bulges and central SMBHs.

However, it is essential to note that the dependence of the stellar population on σ_e is not smooth and monotonic. There is a critical value of $\lg(\sigma_e^{\text{crit}}/\text{km s}^{-1}) \approx 2.3$ (Cappellari 2023) or Σ_1 (Barro et al. 2017; Chen et al. 2020), above which all galaxies are quenched—namely, non-star-forming, old, and metal-rich. For lower σ_e values, there is a large range and a bimodal distribution of population parameters. In particular, there is a clear trend with metallicity $[Z/H]$ being lower for younger galaxies at a given σ_e . This is illustrated in Figure 17 for the final sample of 10K galaxies of the MaNGA survey (Lu et al. 2023).

The (Age, σ_e) diagram is closely related to the color-magnitude diagram (Faber et al. 2007; Schawinski et al. 2014), or the (M_*, SFR) diagram (Brinchmann et al. 2004; Noeske et al. 2007) between stellar mass and star-formation rate (SFR). These diagrams are often used to understand the process of galaxy quenching. The advantage of the (Age, σ_e) diagram is that σ_e , unlike mass M_* or luminosity L , better aligns with the main direction along which galaxy properties vary. This reduces the overlap between different star formation histories of galaxies with different M_* . In this diagram, ETGs are located mainly in the old sequence, at the top of the diagram, equivalent to the red sequence of the color-magnitude diagram. However, below $\lg(\sigma_e/\text{km s}^{-1}) \approx 2.3$, younger ETGs start appearing, having on average lower metallicity and straddling the region populated by spiral galaxies, which tend to lie at the lowest σ_e and lowest metallicities.

The parallelism between the properties of fast rotator ETGs and spiral galaxies in the (M, R_e) plane led Cappellari et al. (2011b) to propose a revision to the classic tuning fork (Hubble 1936) of Figure 1. In this ‘comb diagram’ for galaxy classification, fast rotator ETGs form a parallel sequence to spiral galaxies (Figure 18). Fast rotator ETGs share the same range of disk fractions (S0a–S0c) as spiral galaxies but also extend towards more extreme spheroid-dominated disky-elliptical galaxies E(d)5 (Kormendy & Bender 1996). The nomenclature S0a–S0c for edge-on fast rotators was taken from van den Bergh (1976), who previously suggested a similar parallelism between the subset of S0 alone and spiral galaxies. The difference between the ‘trident’ diagram for E, S0s, and spirals by van den Bergh (1976) and the ‘comb’ diagram for fast/slow rotator ETGs and spirals by Cappellari et al. (2011b) is that, the latter classification is based on kinematics, not photometry: fast rotators also include about 2/3 of the inclined disk galaxies that have been misclassified morphologically as elliptical from photometry alone. These can be recognized at any inclination with stellar kinematics and constitute a much larger class of galaxies than S0s alone. Moreover, the ‘trident’ did not include the extension to E(d) galaxies, which were not known at that time, and can only be detected from photometry when very close to edge-on.

The ‘comb’ diagram in Figure 18 underscores the significance of the variation in the disk-to-total ratio (D/T), and relative disk scale length, within the fast rotator population. On the right side of the ‘comb’ handle are the nearly bulgeless S0c pure-disks fast rotators, resembling thin spiral galaxies stripped of their gas. In the middle are the S0b fast rotators, representing Hubble’s typical S0 galaxies, with a central bulge and a disk dominating at larger radii. The left side of the fast rotator D/T sequence is occupied by the spheroid-dominated fast rotators, which would be classified as disky-elliptical E(d) when viewed edge-on. These galaxies are characterized by stellar disks that dominate the central regions ($R \lesssim R_e$) rather than the outer parts, and spheroids dominating at large radii.

The variation in D/T and the shift from a disk dominating the outer parts to one dominating the central regions can be observed in kinematics at nearly every inclination. Specifically, when the disk dominates at large radii, stellar rotation continues increasing at $R \gtrsim R_e$, whereas when the spheroid dominates at large radii, kinematics show a clear drop at $R \gtrsim R_e$ (see Cappellari 2016, fig. 3). This sequence of D/T in ETGs is illustrated by Graham et al. (2016, fig. 7), who retain the same (but rotated) sequence as the ETGs comb handle of Figure 18, while slightly rearranging spiral galaxies. They propose the term ‘ellicular’ (ES) for what I described as disky-elliptical E(d) fast rotators, characterized by centrally-concentrated disks. A detailed overview of galaxy classification schemes was presented by Graham (2019).

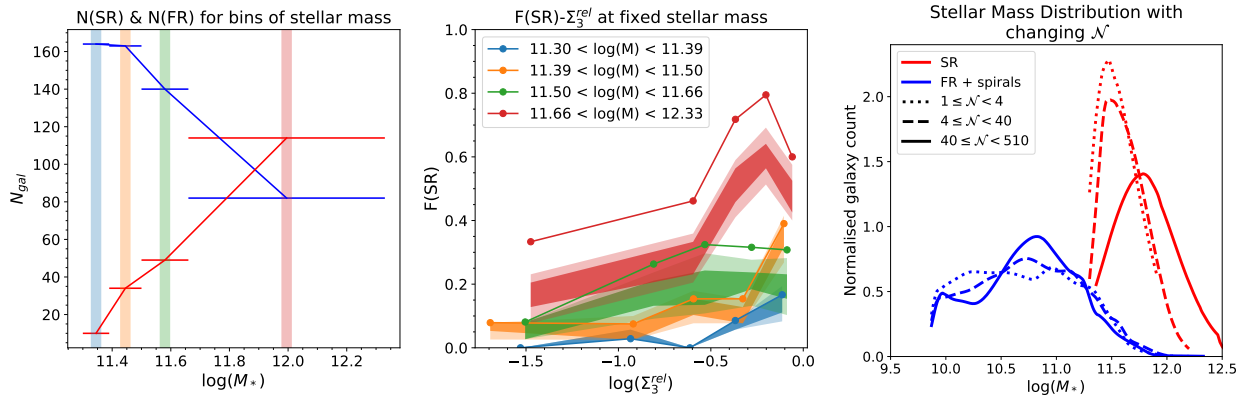


Fig. 19 Left panel: Fraction of fast vs. slow rotators (SRs) among galaxies above the critical mass $\lg(M_*^{\text{crit}}/M_\odot) = 11.3$, as a function of stellar mass. Bins (each containing ~ 200 ETGs) show SR fractions are negligible below M_*^{crit} but rise sharply above it, dominating at $\lg(M_*/M_\odot) \geq 12$. Middle panel: For bins in the left panel, SR fraction $F(\text{SR})$ vs. galaxy number density Σ_3^{rel} (relative to cluster peak density). Shaded bands account for measurement uncertainties in λ_{R_e} and ε_e , addressing misclassification bias. At fixed mass, the most massive SRs preferentially inhabit densest cluster regions. Right panel: Stellar mass probability distributions for massive SRs (red) and non-SR galaxies (blue), split by environment: field (dotted), groups (dashed), clusters (solid). Curves are truncated below the completeness limit. While spirals/fast rotators show no environmental mass dependence, SRs shift to higher masses in denser environments (Graham et al. 2019b, fig. 7, 8).

5 Environmental Dependency of ETGs Properties

Understanding galaxy evolution fundamentally depends on the environment in which galaxies currently exist. Galaxies evolve hierarchically, with their present characteristics influenced by mergers and accretion from their surroundings. Consequently, the environment—typically quantified by the number density of galaxies around a given galaxy down to a certain mass limit—has long been correlated with galaxy properties.

The morphology-density relation is a cornerstone in the study of galaxy evolution, first brought to light by Dressler (1980). This relation reveals a profound connection between the density of a galaxy’s environment and its morphological type. Dressler’s extensive study, which involved observations of over 6000 galaxies across 55 clusters, highlighted a striking pattern: dense environments, such as the crowded centers of galaxy clusters, predominantly host early-type galaxies, including ellipticals and S0s. In stark contrast, spiral galaxies are more frequently found in less dense, more isolated regions.

This discovery underscored the significant influence that a galaxy’s surroundings have on its evolutionary path. In high-density regions, various processes such as ram-pressure stripping, where the interstellar medium is stripped away by interaction with the intracluster medium, and galaxy harassment, involving frequent high-speed encounters between galaxies, contribute to transforming spiral galaxies into ETGs. These mechanisms help explain the scarcity of spiral galaxies in cluster cores.

The implications of the morphology-density relation are far-reaching. It suggests that the environment a galaxy resides in can fundamentally alter its development, affecting not only its structure but also its star formation history, color, and other properties. This has led to a broader understanding that galaxy evolution is a complex interplay between intrinsic properties and external influences.

Despite the many advancements in observational technology and data analysis since 1980, Dressler’s findings have remained remarkably robust. Modern surveys, such as the Sloan Digital Sky Survey (SDSS) with the large Galaxy Zoo sample of morphological classifications of 10^5 galaxies (e.g., Bamford et al. 2009; Skibba et al. 2009), have confirmed the morphology-density relation across different environments. Studies have also shown that the relation extends to redshifts $z \sim 1$ (e.g., Stanford et al. 1998; van Dokkum et al. 2000). JWST is currently pushing the frontier, with some initial indications that environmental effects were already at work up to $z \sim 6$, within one billion years after the Big Bang (e.g., Morishita et al. 2024). This consistency over time suggests that the environment has long played a crucial role in shaping galaxies.

The discovery that the vast majority of elliptical galaxies are actually misclassified S0-like galaxies seen at low inclination, and the realization that this misclassification can be corrected using integral-field stellar kinematics, led to the construction of the *kinematic* morphology-density relation (Cappellari et al. 2011b). This revised relation revealed two key insights:

Genuine Spheroidal Galaxies: Slow rotators are virtually absent in the field or low-density environments. This contrasts with the traditional morphology-density relation, which suggested that the field contained about 10% of (now known to be misclassified) elliptical galaxies.

Distribution of Slow Rotators: The fraction of slow rotators does not vary gradually with environmental density. Instead, massive slow rotators are almost exclusively found at the density peaks of groups and clusters (Cappellari et al. 2011b; Cappellari 2013; Scott et al. 2014; D’Eugenio et al. 2013; Fogarty et al. 2014).

Subsequent analyses from the SAMI and MaNGA surveys initially appeared to challenge earlier findings by reporting *no significant*

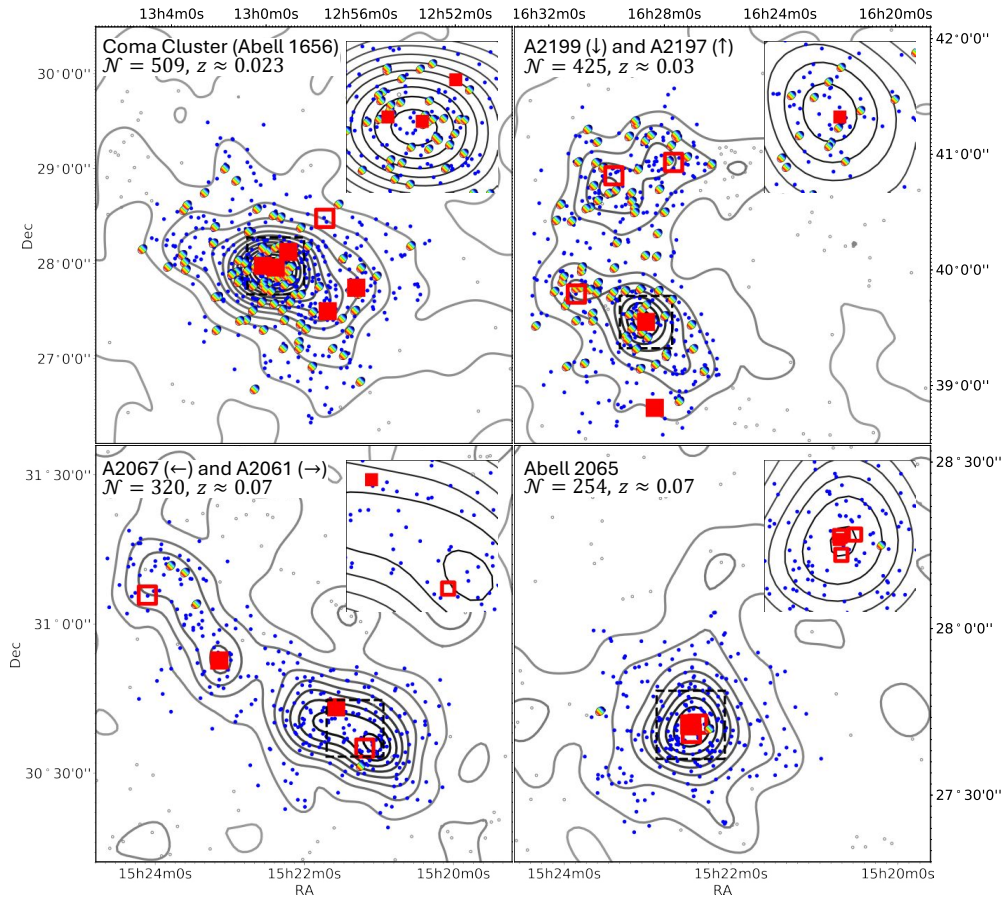


Fig. 20 Galaxy clusters with MaNGA kinematics. Cluster members: red squares = slow rotators (SRs) with $M_* > M_*^{\text{crit}} = 2 \times 10^{11} M_{\odot}$; blue circles = other galaxies. Filled symbols denote FR/SR classifications from integral-field kinematics; unfilled symbols indicate photometric classifications. Gray unfilled circles are non-members. Contours show the kernel density estimate (KDE) of galaxy number density. Each panel (1 Mpc² field of view, centered on the densest peak; inset zooms in on core) lists the Abell designation, member count (N), and redshift (z). SRs are rare and preferentially located near density peaks, particularly in unrelaxed clusters with multiple subpeaks (each often hosting an SR). Top Left: Coma Cluster (A1656) with three SRs at its core. Top Right: A2197 and A2199. A2197’s bimodal velocity distribution suggests two interacting subclusters: A2197W and A2197E. Bottom Left: A2061 (lower right) and A2067 (upper left) in the Corona Borealis Supercluster (CBS), likely gravitationally bound. Bottom Right: A2065 (CBS). (Graham et al. 2019a, fig. 1)

environmental dependence of early-type galaxy (ETG) kinematics when controlling for stellar mass (Brough et al. 2017; Greene et al. 2017; Veale et al. 2017). These studies argued that stellar mass alone governs λ_{R_c} evolution, with environment playing negligible role. However, this interpretation overlooks a critical coupling: galaxy mass growth and angular momentum loss are inherently linked processes driven by mergers. Environmental effects (e.g., cluster vs. field habitats) modulate merger rates, which simultaneously drive (i) stellar mass growth through mergers and (ii) angular momentum decrease via dynamical heating.

This coupling naturally explains the initially observed insignificant λ_{R_c} –environment trends *at fixed M_** – galaxies cannot lose angular momentum without gaining mass through the same environmental processes. Furthermore, three limitations compound this null result: (i) slow rotators are intrinsically rare, reducing statistical power; (ii) environmental metrics (e.g., halo mass, local density) carry large systematic uncertainties.

A biological analogy clarifies this problem: attempting to detect environmental effects on human height *at fixed weight* would be equally challenging. Environment modulates growth processes that simultaneously increase both height (through nutrition) and weight (through calorie intake) during development. Just as childhood nutrition affects adult stature *through* its association with weight gain, galaxy environments shape λ_{R_c} *through* their role in mass assembly. Expecting strong environmental signatures at fixed M_* is thus both statistically and physically ill-posed – the two parameters represent different facets of the same evolutionary history. The apparent contradiction between

studies instead reinforces the unified λ_{R_e} and M_* evolutionary sequence predicted by hierarchical models.

Later, more detailed analysis of both MaNGA and SAMI survey data uncovered the expected weak *residual* trends of ETG kinematics as a function of environment, *at fixed stellar mass*, on top of the well-established major dependency as a function of mass (Graham et al. 2019b; van de Sande et al. 2021b). This is illustrated in Figure 19: the left panel shows the main trend, with the fraction of slow rotator ETGs increasing sharply above the critical mass stellar $M_*^{\text{crit}} \approx 2 \times 10^{11} M_\odot$ (Cappellari 2016) and dominating at $M_* \sim 10^{12} M_\odot$. In the figures, each mass bin was chosen to contain the same number of about 200 galaxies, to ensure that number statistics do not impact any observed difference. The middle panel shows how the fraction of slow rotators increases with environmental density *at fixed stellar mass*. Especially in the largest mass bins, where the fraction of slow rotators is larger, there is a clear increase as a function of environment. The right panel shows the mass function of fast/slow rotator ETGs for three environmental densities. It shows that, while the fraction of fast rotators and spirals is independent of environmental density, the mass function of slow rotators changes as a function of environment, shifting towards the largest masses in the densest environments. A similar result was shown for a complete but smaller sample, with different data, in Cappellari (2013, fig. 4).

Given the rarity of slow rotators in clusters, a more direct way of understanding the effect of the environment on their distribution can be obtained by directly looking at a small set of well-studied clusters. This is illustrated in Figure 20, where the slow rotators appear to trace the peaks of the density distribution in clusters. Given that clusters form hierarchically by the merging of smaller groups, the fact that slow rotators lie close to the density of substructure suggests they were already formed in the smaller groups before these merged to form larger clusters. Similar slow rotator ETG distributions were shown with complete kinematic coverage for the well-studied Fornax and Virgo clusters in the review by Cappellari (2016, fig. 26) and with more sparse kinematic coverage in eight clusters by Brough et al. (2017).

6 Formation and Evolution: A Tale of Two Paths

The bimodal distribution of the photometric and kinematic properties of early-type galaxies (ETGs) reflects the different channels shaping their evolution. Comprehensive reviews of galaxy formation and key challenges are provided by Somerville & Davé (2015) and Naab & Ostriker (2017), while Cappellari (2016) reviews specifically the evolutionary paths of fast and slow rotator ETGs. To understand the distinct properties of fast and slow rotator ETGs, we must consider the hierarchical growth of galaxies, clusters, and their dark halos (Mo et al. 2010).

In the early universe, primordial density fluctuations led to the formation of dark matter halos, which attracted and accumulated gas. As the gas cooled and condensed, it formed rotating disks that eventually became spiral galaxies (White & Rees 1978). The most massive halos, created from the largest density fluctuations, attracted gas at much higher rates due to their strong gravitational pull. This resulted in violent disk instability, nuclear gas inflows, and intense star formation. The resulting supernova explosions from massive stars caused strong feedback on the gas and enhanced the α elements. Additionally, when halos exceeded a critical mass, the infalling gas was shock-heated (Kereš et al. 2005; Dekel & Birnboim 2006).

At the centers of these massive halos, supermassive black holes grow from pre-existing seeds, accreting gas and producing jets that inject energy into the surrounding medium (e.g., Dubois et al. 2016; Nelson et al. 2019). Initial indications from JWST (Maiolino et al. 2024) suggest that by redshift $4 \lesssim z \lesssim 7$, black holes lie on the local relation between stellar and black hole mass. These combined feedback effects rapidly suppress star formation, leading to the formation of the precursors of slow rotator ETGs, situated at the centers of their massive dark halos and surrounded by hot gas glowing in X-rays (e.g., Bender et al. 1989). Due to intense and chaotic gas accretion and gas disk disruption, these massive galaxies are characterized by their spheroidal shapes, lack of stellar disks, and low specific angular momentum.

The subsequent evolution of slow rotators follows the hierarchical growth of galaxy groups into larger clusters (e.g., De Lucia et al. 2012). Because slow rotators quench their star formation early and inhabit environments hostile to further cold gas accretion, their evolution is dominated by gas-poor (dry) mergers. With their large masses and low relative velocities within their halos, slow rotators have large collisional cross-sections. Consequently, when their host groups or clusters merge, they also merge efficiently while also accreting smaller quenched galaxies, forming even more massive slow rotators (e.g., Choi et al. 2018). These massive slow rotators have extended outer stellar halos and high Sérsic indices (Figure 3) due to the deposition of accreted stars at large radii (e.g., Naab et al. 2009; Pillepich et al. 2018). During gas-free mergers, galaxies are expected to move along lines with $M_* \propto R_e$ (or slightly steeper) (Naab et al. 2009; Bezanson et al. 2009), without altering their chemical composition since no new star formation is involved. This explains the near-constancy of galaxy properties along lines of constant $\sigma_e \propto \sqrt{M_*/R_e}$ on the (M_*, R_e) diagram (Figure 15, Figure 16). The growth in size (e.g., Trujillo et al. 2006; van der Wel et al. 2014) and Sérsic index of massive galaxies can be traced as a function of redshift (e.g., van Dokkum et al. 2010) (see review in Cappellari 2016, sec. 6).

When slow rotators merge, their supermassive black holes sink to the center of the remnant through dynamical friction, forming a black hole binary that eventually merges to produce a larger black hole, while emitting detectable gravitational waves. During this process, the black hole binary ejects stars on radial orbits (Milosavljević & Merritt 2001; Rantala et al. 2024), leaving a ‘scoured’ flattened inner stellar core (Figure 3) with a tangentially-biased nuclear stellar orbital distribution (Figure 10). This hierarchical growth process, including the two-phase evolution with intense in-situ star formation followed by dry merger accretion (Oser et al. 2010), can accurately reproduce the observed properties of slow rotators (Rantala et al. 2024), including their location at cluster density peaks (Figure 20). The significant enhancement in α elements (Krajinović et al. 2020) provides a glimpse into the early epoch of highly efficient star formation within these massive halos at high redshift.

In contrast, gas-rich disk galaxies in lower-density environments evolve more gradually (e.g., Pillepich et al. 2019). These galaxies may undergo gas-rich mergers, triggering bursts of star formation and leading to the formation of stellar bulges as gas dissipates and sinks into their centers. During these mergers, stellar density increases near the centers, the central SMBH grows by accretion, and the stellar

populations evolve due to fresh star formation and chemical recycling, increasing their metallicity. This implies that these galaxies will cross lines of constant $\sigma_e \propto \sqrt{M_*/R_e}$, from left to right (Figure 16; Cappellari 2016, fig. 29). However, as these galaxies evolve, they may become quiescent (quenched) due to internal feedback mechanisms, such as AGN activity and stellar winds from supernova explosions. Empirical evidence of this quenching process out to $z \sim 3$ has been detected with JWST (D'Eugenio et al. 2024a). These passive galaxies, the fast rotator ETGs, are characterized by their disk-like morphologies (like S0s or disky ellipticals, when seen edge-on) and high specific stellar angular momentum.

The environmental impact on the evolution of galaxies with low and intermediate masses is profound. Disk galaxies are uniformly scattered inside groups and clusters with relative low masses, large relative velocities and consequently small collisional cross section. In dense environments, like galaxy clusters, they are subjected to tidal forces and ram pressure stripping, which can remove their gas and quench star formation (see reviews by Boselli & Gavazzi 2006; Cortese et al. 2021). Combined with internal processes, these environmental effects transform disk galaxies into fast rotator ETGs, which may subsequently accrete more mass through minor mergers. This is evidenced, for instance, by integral-field spectroscopic observations showing galaxy disks with lower metallicity than their bulges, likely indicating fresh, low-metallicity gas accretion (Lu et al. 2023).

While this simplified picture provides a framework for understanding ETG formation and evolution, the reality is more complex. Various factors, including initial conditions, merger history, and environmental influences, shape these galaxies' final properties. Future observations and simulations will continue to illuminate the intricate processes that govern the birth and evolution of early-type galaxies.

7 Summary and Outlook

In this chapter, I have shown that early-type galaxies (ETGs) are not a homogeneous class but display a bimodal distribution in key structural properties, particularly in their stellar specific angular momentum, kinematic morphology, and nuclear surface brightness profiles.

Slow Rotator ETGs: This class of ETGs tends to be found at the peaks of local overdensities in galaxy clusters. There is a strong dependency between stellar mass and specific angular momentum. Slow rotators are nearly absent at low mass but start to dominate above a characteristic stellar mass of $M_*^{\text{crit}} \approx 2 \times 10^{11} M_\odot$. They are generally close to spherical or mildly triaxial within $1R_e$ and can become significantly flattened only in their outer stellar halos. These galaxies are metal-rich, composed of stars nearly as old as the Universe, and enhanced in α elements, indicating they formed most of their stars quickly and efficiently at high redshift, growing primarily through gas-poor mergers.

Fast Rotator ETGs: This class is closely related to spiral galaxies, forming a continuous sequence of properties with them. The structure of fast rotator ETGs cannot be understood without considering spiral galaxies. Empirically, this sequence starts with star-forming spiral galaxies, continues with S0 galaxies, and ends with the most spheroid-dominated disky elliptical galaxies. The empirical global parameter that best traces this sequence is the stellar velocity dispersion σ_e . Equally effective tracers of this sequence from spiral to fast rotator ETGs include the virial estimator of σ_e (inferred from stellar mass and size using $\sigma_e \propto \sqrt{M_*/R_e}$) or the surface density Σ_1 within 1 kpc. There is a critical value of $\lg(\sigma_e^{\text{crit}} / \text{km s}^{-1}) \approx 2.3$, above which all ETGs are quenched, passive, and metal-rich. However, below σ_e^{crit} , this parameter does not fully capture the variation in galaxy properties; instead, at smaller σ_e values, there is a spread in age at fixed σ_e , with a clear trend for younger galaxies to have lower metallicity.

The distribution of fast/slow rotator ETGs and spiral galaxies as a function of their environment, their structural differences, and the modeling of galaxy evolution via numerical simulations indicates two broadly distinct paths for their formation. Slow rotators form most of their stars early and rapidly in the Universe's evolution. They quench quickly and subsequently remain passive for most of their evolution, growing via dry mergers and following the hierarchical growth of their host groups/clusters. Fast rotators start as star-forming disks, growing more gradually over time. Their bulges and supermassive black holes co-evolve, fed by accreted gas, until they are quenched by internal feedback or environmental factors.

Our understanding of ETGs' structure and evolution is built on a synergy between detailed local observations, mainly from integral-field spectroscopy, and less detailed observations at higher redshifts, generally involving photometry alone. To test the evolutionary scenario, we need integral-field spectroscopy observations at higher redshifts. Until now, these have been beyond the reach of current instrumentation. However, with the launch of JWST, high-spatial-resolution integral-field spectroscopy is now possible. This allows for spatially-resolved stellar kinematics up to redshift $z \sim 2$, at the critical time when most of the mass is being assembled. In a few years, the Extremely Large Telescope will enable even higher spatial resolution integral-field spectroscopy, promising a new revolution in galaxy formation studies.

References

- Auger M. W., Treu T., Bolton A. S., Gavazzi R., Koopmans L. V. E., Marshall P. J., Moustakas L. A., Burles S., 2010, "The Sloan Lens ACS Survey. X. Stellar, Dynamical, and Total Mass Correlations of Massive Early-type Galaxies", *ApJ*, **724**, 511
- Bamford S. P. et al., 2009, "Galaxy Zoo: the dependence of morphology and colour on environment", *MNRAS*, **393**, 1324
- Barone T. M. et al., 2018, "The SAMI Galaxy Survey: Gravitational Potential and Surface Density Drive Stellar Populations. I. Early-type Galaxies", *ApJ*, **856**, 64

- Barrera-Ballesteros J. K. et al., 2015, “Tracing kinematic (mis)alignments in CALIFA merging galaxies. Stellar and ionized gas kinematic orientations at every merger stage”, *A&A*, **582**, A21
- Barro G. et al., 2017, “Structural and Star-forming Relations since $z \sim 3$: Connecting Compact Star-forming and Quiescent Galaxies”, *ApJ*, **840**, 47
- Bell E. F. et al., 2012, “What Turns Galaxies Off? The Different Morphologies of Star-forming and Quiescent Galaxies since $z \sim 2$ from CANDELS”, *ApJ*, **753**, 167
- Bender R., 1988, “Velocity anisotropies and isophote shapes in elliptical galaxies”, *A&A*, **193**, L7
- Bender R., Surma P., Doebereiner S., Moellenhoff C., Madejsky R., 1989, “Isophote shapes of elliptical galaxies. II - Correlations with global optical, radio and X-ray properties”, *A&A*, **217**, 35
- Bernardi M. et al., 2003, “Early-Type Galaxies in the Sloan Digital Sky Survey. III. The Fundamental Plane”, *AJ*, **125**, 1866
- Bezanson R., van Dokkum P. G., Tal T., Marchesini D., Kriek M., Franx M., Coppi P., 2009, “The Relation Between Compact, Quiescent High-redshift Galaxies and Massive Nearby Elliptical Galaxies: Evidence for Hierarchical, Inside-Out Growth”, *ApJ*, **697**, 1290
- Binney J., 2005, “Rotation and anisotropy of galaxies revisited”, *MNRAS*, **363**, 937
- Binney J., Mamon G. A., 1982, “M/L and velocity anisotropy from observations of spherical galaxies, or must M87 have a massive black hole?”, *MNRAS*, **200**, 361
- Binney J., Tremaine S., 2008, *Galactic Dynamics: Second Edition*, Princeton University Press, Princeton, NJ
- Bland-Hawthorn J., Tepper-Garcia T., Agertz O., Federrath C., 2024, “Turbulent Gas-rich Disks at High Redshift: Bars and Bulges in a Radial Shear Flow”, *ApJ*, **968**, 86
- Blumenthal G. R., Faber S. M., Primack J. R., Rees M. J., 1984, “Formation of galaxies and large-scale structure with cold dark matter”, *Nature*, **311**, 517
- Bolton A. S., Burles S., Treu T., Koopmans L. V. E., Moustakas L. A., 2007, “A More Fundamental Plane”, *ApJ*, **665**, L105
- Boselli A., Gavazzi G., 2006, “Environmental Effects on Late-Type Galaxies in Nearby Clusters”, *PASP*, **118**, 517
- Brinchmann J., Charlot S., White S. D. M., Tremonti C., Kauffmann G., Heckman T., Brinkmann J., 2004, “The physical properties of star-forming galaxies in the low-redshift Universe”, *MNRAS*, **351**, 1151
- Brough S. et al., 2017, “The SAMI Galaxy Survey: Mass as the Driver of the Kinematic Morphology-Density Relation in Clusters”, *ApJ*, **844**, 59
- Caon N., Capaccioli M., D’Onofrio M., 1993, “On the Shape of the Light Profiles of Early Type Galaxies”, *MNRAS*, **265**, 1013
- Cappellari M., 2002, “Efficient multi-Gaussian expansion of galaxies”, *MNRAS*, **333**, 400
- Cappellari M., 2008, “Measuring the inclination and mass-to-light ratio of axisymmetric galaxies via anisotropic Jeans models of stellar kinematics”, *MNRAS*, **390**, 71
- Cappellari M., 2013, “Effect of Environment on Galaxies’ Mass-Size Distribution: Unveiling the Transition from outside-in to inside-out Evolution”, *ApJ*, **778**, L2
- Cappellari M., 2016, “Structure and Kinematics of Early-Type Galaxies from Integral Field Spectroscopy”, *ARA&A*, **54**, 597
- Cappellari M., 2020, “Efficient solution of the anisotropic spherically aligned axisymmetric Jeans equations of stellar hydrodynamics for galactic dynamics”, *MNRAS*, **494**, 4819
- Cappellari M., 2023, “Full spectrum fitting with photometry in PPXF: stellar population versus dynamical masses, non-parametric star formation history and metallicity for 3200 LEGA-C galaxies at redshift $z \approx 0.8$ ”, *MNRAS*, **526**, 3273
- Cappellari M., Copin Y., 2003, “Adaptive spatial binning of integral-field spectroscopic data using Voronoi tessellations”, *MNRAS*, **342**, 345
- Cappellari M. et al., 2006, “The SAURON project - IV. The mass-to-light ratio, the virial mass estimator and the Fundamental Plane of elliptical and lenticular galaxies”, *MNRAS*, **366**, 1126
- Cappellari M. et al., 2007, “The SAURON project - X. The orbital anisotropy of elliptical and lenticular galaxies: revisiting the $(V/\sigma, \epsilon)$ diagram with integral-field stellar kinematics”, *MNRAS*, **379**, 418
- Cappellari M. et al., 2008, “Supermassive black holes from OASIS and SAURON integral-field kinematics”, *Formation and Evolution of Galaxy Bulges*, pp. 215–218
- Cappellari M. et al., 2011a, “The ATLAS^{3D} project - I. A volume-limited sample of 260 nearby early-type galaxies: science goals and selection criteria”, *MNRAS*, **413**, 813
- Cappellari M. et al., 2011b, “The ATLAS^{3D} project - VII. A new look at the morphology of nearby galaxies: the kinematic morphology-density relation”, *MNRAS*, **416**, 1680
- Cappellari M. et al., 2012, “Systematic variation of the stellar initial mass function in early-type galaxies”, *Nature*, **484**, 485
- Cappellari M. et al., 2013a, “The ATLAS^{3D} project - XV. Benchmark for early-type galaxies scaling relations from 260 dynamical models: mass-to-light ratio, dark matter, Fundamental Plane and Mass Plane”, *MNRAS*, **432**, 1709
- Cappellari M. et al., 2013b, “The ATLAS^{3D} project - XX. Mass-size and mass- σ distributions of early-type galaxies: bulge fraction drives kinematics, mass-to-light ratio, molecular gas fraction and stellar initial mass function”, *MNRAS*, **432**, 1862
- Cappellari M. et al., 2015, “Small Scatter and Nearly Isothermal Mass Profiles to Four Half-light Radii from Two-dimensional Stellar Dynamics of Early-type Galaxies”, *ApJ*, **804**, L21
- Chen Z. et al., 2020, “Quenching as a Contest between Galaxy Halos and Their Central Black Holes”, *ApJ*, **897**, 102

- Cheung E. et al., 2012, “The Dependence of Quenching upon the Inner Structure of Galaxies at $0.5 < z < 0.8$ in the DEEP2/AEGIS Survey”, *ApJ*, **760**, 131
- Choi H., Yi S. K., Dubois Y., Kimm T., Devriendt J. E. G., Pichon C., 2018, “Early-type Galaxy Spin Evolution in the Horizon-AGN Simulation”, *ApJ*, **856**, 114
- Colless M., Saglia R. P., Burstein D., Davies R. L., McMahan R. K., Wegner G., 2001, “The peculiar motions of early-type galaxies in two distant regions - VII. Peculiar velocities and bulk motions”, *MNRAS*, **321**, 277
- Cortese L., Catinella B., Smith R., 2021, “The Dawes Review 9: The role of cold gas stripping on the star formation quenching of satellite galaxies”, *Publ. Astron. Soc. Australia*, **38**, e035
- Cortese L. et al., 2022, “The physical connection between central stellar surface density and stellar spin in SAMI and MaNGA nearby galaxies”, *MNRAS*, **513**, 3709
- Courteau S. et al., 2014, “Galaxy masses”, *Reviews of Modern Physics*, **86**, 47
- D’Eugenio F., Houghton R. C. W., Davies R. L., Dalla Bontà E., 2013, “Fast and slow rotators in the densest environments: a FLAMES/GIRAFFE integral field spectroscopy study of galaxies in A1689 at $z = 0.183$ ”, *MNRAS*, **429**, 1258
- D’Eugenio F. et al., 2021, “The SAMI Galaxy Survey: stellar population and structural trends across the Fundamental Plane”, *MNRAS*, **504**, 5098
- D’Eugenio F. et al., 2024a, “A fast-rotator post-starburst galaxy quenched by supermassive black-hole feedback at $z = 3$ ”, *Nature Astronomy*, **8**, 1443
- D’Eugenio F. et al., 2024b, “The hyperplane of early-type galaxies: using stellar population properties to increase the precision and accuracy of the fundamental plane as a distance indicator”, *MNRAS*, **532**, 1775
- De Lucia G., Weinmann S., Poggianti B. M., Aragón-Salamanca A., Zaritsky D., 2012, “The environmental history of group and cluster galaxies in a Λ cold dark matter universe”, *MNRAS*, **423**, 1277
- Dekel A., Birnboim Y., 2006, “Galaxy bimodality due to cold flows and shock heating”, *MNRAS*, **368**, 2
- Dekel A., Ginzburg O., Jiang F., Freundlich J., Lapiner S., Ceverino D., Primack J., 2020, “A mass threshold for galactic gas discs by spin flips”, *MNRAS*, **493**, 4126
- De Vaucouleurs G., 1948, “Recherches sur les Nebuleuses Extragalactiques”, *Annales d’Astrophysique*, **11**, 247
- Djorgovski S., Davis M., 1987, “Fundamental properties of elliptical galaxies”, *ApJ*, **313**, 59
- Dressler A., 1980, “Galaxy morphology in rich clusters - Implications for the formation and evolution of galaxies”, *ApJ*, **236**, 351
- Dressler A., Lynden-Bell D., Burstein D., Davies R. L., Faber S. M., Terlevich R., Wegner G., 1987, “Spectroscopy and photometry of elliptical galaxies. I - A new distance estimator”, *ApJ*, **313**, 42
- Dubois Y., Peirani S., Pichon C., Devriendt J., Gavazzi R., Welker C., Volonteri M., 2016, “The HORIZON-AGN simulation: morphological diversity of galaxies promoted by AGN feedback”, *MNRAS*, **463**, 3948
- Dutton A. A., Treu T., 2014, “The bulge-halo conspiracy in massive elliptical galaxies: implications for the stellar initial mass function and halo response to baryonic processes”, *MNRAS*, **438**, 3594
- Emsellem E., Monnet G., Bacon R., 1994, “The multi-gaussian expansion method: a tool for building realistic photometric and kinematical models of stellar systems I. The formalism”, *A&A*, **285**, 723
- Emsellem E. et al., 2004, “The SAURON project - III. Integral-field absorption-line kinematics of 48 elliptical and lenticular galaxies”, *MNRAS*, **352**, 721
- Emsellem E. et al., 2007, “The SAURON project - IX. A kinematic classification for early-type galaxies”, *MNRAS*, **379**, 401
- Emsellem E. et al., 2011, “The ATLAS^{3D} project - III. A census of the stellar angular momentum within the effective radius of early-type galaxies: unveiling the distribution of fast and slow rotators”, *MNRAS*, **414**, 888
- Faber S. M., Jackson R. E., 1976, “Velocity dispersions and mass-to-light ratios for elliptical galaxies.” *ApJ*, **204**, 668
- Faber S. M. et al., 1997, “The Centers of Early-Type Galaxies with HST. IV. Central Parameter Relations.” *AJ*, **114**, 1771
- Faber S. M. et al., 2007, “Galaxy Luminosity Functions to $z \sim 1$ from DEEP2 and COMBO-17: Implications for Red Galaxy Formation”, *ApJ*, **665**, 265
- Falcón-Barroso J. et al., 2011, “The SAURON project - XIX. Optical and near-infrared scaling relations of nearby elliptical, lenticular and Sa galaxies”, *MNRAS*, **417**, 1787
- Falcón-Barroso J. et al., 2019, “The CALIFA view on stellar angular momentum across the Hubble sequence”, *A&A*, **632**, A59
- Fang J. J., Faber S. M., Koo D. C., Dekel A., 2013, “A Link between Star Formation Quenching and Inner Stellar Mass Density in Sloan Digital Sky Survey Central Galaxies”, *ApJ*, **776**, 63
- Ferrarese L., van den Bosch F. C., Ford H. C., Jaffe W., O’Connell R. W., 1994, “Hubble Space Telescope photometry of the central regions of Virgo cluster elliptical galaxies. 3: Brightness profiles”, *AJ*, **108**, 1598
- Fogarty L. M. R. et al., 2014, “The SAMI Pilot Survey: the kinematic morphology-density relation in Abell 85, Abell 168 and Abell 2399”, *MNRAS*, **443**, 485
- Franx M., van Dokkum P. G., Schreiber N. M. F., Wuyts S., Labbé I., Toft S., 2008, “Structure and Star Formation in Galaxies out to $z = 3$: Evidence for Surface Density Dependent Evolution and Upsizing”, *ApJ*, **688**, 770
- Freeman K. C., 1970, “On the Disks of Spiral and so Galaxies”, *ApJ*, **160**, 811
- Gebhardt K. et al., 2003, “Axisymmetric Dynamical Models of the Central Regions of Galaxies”, *ApJ*, **583**, 92
- Gebhardt K., Adams J., Richstone D., Lauer T. R., Faber S. M., Gültekin K., Murphy J., Tremaine S., 2011, “The Black Hole Mass in M87 from Gemini/NIFS Adaptive Optics Observations”, *ApJ*, **729**, 119

- Gerhard O., Kronawitter A., Saglia R. P., Bender R., 2001, “Dynamical Family Properties and Dark Halo Scaling Relations of Giant Elliptical Galaxies”, *AJ*, **121**, 1936
- Gerhard O. E., 1993, “Line-of-sight velocity profiles in spherical galaxies: breaking the degeneracy between anisotropy and mass.” *MNRAS*, **265**, 213
- Gerhard O. E., Binney J. J., 1996, “On the deprojection of axisymmetric bodies”, *MNRAS*, **279**, 993
- Gnedin O. Y., Kravtsov A. V., Klypin A. A., Nagai D., 2004, “Response of Dark Matter Halos to Condensation of Baryons: Cosmological Simulations and Improved Adiabatic Contraction Model”, *ApJ*, **616**, 16
- Graham A. W., Erwin P., Trujillo I., Asensio Ramos A., 2003, “A New Empirical Model for the Structural Analysis of Early-Type Galaxies, and A Critical Review of the Nuker Model”, *AJ*, **125**, 2951
- Graham A. W., 2019, “A galaxy classification grid that better recognizes early-type galaxy morphology”, *MNRAS*, **487**, 4995
- Graham A. W., Ciambur B. C., Savorgnan G. A. D., 2016, “Disk Elliptical Galaxies and the Allegedly Over-massive Black Hole in the Compact “ES” Galaxy NGC 1271”, *ApJ*, **831**, 132
- Graham M. T., Cappellari M., Bershadly M. A., Drory N., 2019a, “Complete census of massive slow rotators in ten large galaxy clusters”, *arXiv e-prints*, [arXiv:1911.06103](https://arxiv.org/abs/1911.06103)
- Graham M. T., Cappellari M., Bershadly M. A., Drory N., 2019b, “SDSS-IV MaNGA: New benchmark for the connection between stellar angular momentum and environment: a study of about 900 groups/clusters”, *arXiv e-prints*, [arXiv:1910.05139](https://arxiv.org/abs/1910.05139)
- Graham M. T. et al., 2018, “SDSS-IV MaNGA: stellar angular momentum of about 2300 galaxies: unveiling the bimodality of massive galaxy properties”, *MNRAS*, **477**, 4711
- Graves G. J., Faber S. M., Schiavon R. P., 2009, “Dissecting the Red Sequence. II. Star Formation Histories of Early-Type Galaxies Throughout the Fundamental Plane”, *ApJ*, **698**, 1590
- Greene J. E. et al., 2017, “SDSS-IV MaNGA: Probing the Kinematic Morphology-Density Relation of Early-type Galaxies with MaNGA”, *ApJ*, **851**, L33
- Hubble E. P., 1926, “Extragalactic nebulae.” *ApJ*, **64**, 321
- Hubble E. P., 1936, *Realm of the Nebulae*, Yale Univ. Press, New Haven
- Jeans J. H., 1922, “The Motions of Stars in a Kapteyn Universe”, *MNRAS*, **82**, 122
- Jeans J. H., 1928, *Astronomy and cosmogony*, Cambridge Univ. Press
- Jin Y., Zhu L., Long R. J., Mao S., Xu D., Li H., van de Ven G., 2019, “Evaluating the ability of triaxial Schwarzschild modelling to estimate properties of galaxies from the Illustris simulation”, *MNRAS*, **486**, 4753
- Kereš D., Katz N., Weinberg D. H., Davé R., 2005, “How do galaxies get their gas?”, *MNRAS*, **363**, 2
- Koopmans L. V. E. et al., 2009, “The Structure and Dynamics of Massive Early-Type Galaxies: On Homology, Isothermality, and Isotropy Inside One Effective Radius”, *ApJ*, **703**, L51
- Kormendy J., 1977, “Brightness distributions in compact and normal galaxies. II - Structure parameters of the spheroidal component”, *ApJ*, **218**, 333
- Kormendy J., Bender R., 1996, “A Proposed Revision of the Hubble Sequence for Elliptical Galaxies”, *ApJ*, **464**, L119
- Kormendy J., Fisher D. B., Cornell M. E., Bender R., 2009, “Structure and Formation of Elliptical and Spheroidal Galaxies”, *ApJS*, **182**, 216
- Kormendy J., Ho L. C., 2013, “Coevolution (Or Not) of Supermassive Black Holes and Host Galaxies”, *ARA&A*, **51**, 511
- Krajnović D., Cappellari M., de Zeeuw P. T., Copin Y., 2006, “Kinemetry: a generalization of photometry to the higher moments of the line-of-sight velocity distribution”, *MNRAS*, **366**, 787
- Krajnović D. et al., 2011, “The ATLAS^{3D} project - II. Morphologies, kinematic features and alignment between photometric and kinematic axes of early-type galaxies”, *MNRAS*, **414**, 2923
- Krajnović D. et al., 2013, “The ATLAS^{3D} Project - XXIII. Angular momentum and nuclear surface brightness profiles”, *MNRAS*, **433**, 2812
- Krajnović D. et al., 2018, “A quartet of black holes and a missing duo: probing the low end of the $M_{BH} - \sigma$ relation with the adaptive optics assisted integral-field spectroscopy”, *MNRAS*, **477**, 3030
- Krajnović D. et al., 2020, “Formation channels of slowly rotating early-type galaxies”, *A&A*, **635**, A129
- Lauer T. R., 2012, “Cores and the Kinematics of Early-type Galaxies”, *ApJ*, **759**, 64
- Lauer T. R. et al., 1995, “The Centers of Early-Type Galaxies with HST.I. An Observational Survey”, *AJ*, **110**, 2622
- Leung G. Y. C. et al., 2018, “The EDGE-CALIFA survey: validating stellar dynamical mass models with CO kinematics”, *MNRAS*, **477**, 254
- Li H., Mao S., Cappellari M., Graham M. T., Emsellem E., Long R. J., 2018a, “SDSS-IV MaNGA: The Intrinsic Shape of Slow Rotator Early-type Galaxies”, *ApJ*, **863**, L19
- Li H. et al., 2018b, “SDSS-IV MaNGA: global stellar population and gradients for about 2000 early-type and spiral galaxies on the mass-size plane”, *MNRAS*, **476**, 1765
- Li R. et al., 2019, “SDSS-IV MaNGA: the inner density slopes of nearby galaxies”, *MNRAS*, **490**, 2124
- Li S., Li R., Zhu K., Lu S., Cappellari M., Mao S., Wang C., Gao L., 2024, “MaNGA DynPop - VI. Matter density slopes from dynamical models of 6000 galaxies versus cosmological simulations: the interplay between baryonic and dark matter”, *MNRAS*, **529**, 4633

- Lu S., Zhu K., Cappellari M., Li R., Mao S., Xu D., 2023, “MaNGA DynPop - II. Global stellar population, gradients, and star-formation histories from integral-field spectroscopy of 10K galaxies: link with galaxy rotation, shape, and total-density gradients”, *MNRAS*, **526**, 1022
- Lu S., Zhu K., Cappellari M., Li R., Mao S., Xu D., 2024, “MaNGA DynPop - V. The dark-matter fraction versus stellar velocity dispersion relation and stellar initial mass function variations in galaxies: dynamical models and full spectrum fitting of integral-field spectroscopy”, *MNRAS*, **530**, 4474
- Magoulas C. et al., 2012, “The 6dF Galaxy Survey: the near-infrared Fundamental Plane of early-type galaxies”, *MNRAS*, **427**, 245
- Maiolino R. et al., 2024, “JADES: The diverse population of infant black holes at $4 < z < 11$: Merging, tiny, poor, but mighty”, *A&A*, **691**, A145
- Mandelbaum R., 2018, “Weak Lensing for Precision Cosmology”, *ARA&A*, **56**, 393
- McDermid R. M. et al., 2015, “The ATLAS^{3D} Project - XXX. Star formation histories and stellar population scaling relations of early-type galaxies”, *MNRAS*, **448**, 3484
- Milosavljević M., Merritt D., 2001, “Formation of Galactic Nuclei”, *ApJ*, **563**, 34
- Mo H., van den Bosch F. C., White S., 2010, *Galaxy Formation and Evolution*, Cambridge Univ. Press
- Morishita T. et al., 2024, “Accelerated Emergence of Evolved Galaxies in Early Overdensities at $z \sim 5.7$ ”, *arXiv e-prints*, [arXiv:2408.10980](https://arxiv.org/abs/2408.10980)
- Naab T., Johansson P. H., Ostriker J. P., 2009, “Minor Mergers and the Size Evolution of Elliptical Galaxies”, *ApJ*, **699**, L178
- Naab T., Ostriker J. P., 2017, “Theoretical Challenges in Galaxy Formation”, *ARA&A*, **55**, 59
- Navarro J. F., Frenk C. S., White S. D. M., 1996, “The Structure of Cold Dark Matter Halos”, *ApJ*, **462**, 563
- Nelson D. et al., 2019, “First results from the TNG50 simulation: galactic outflows driven by supernovae and black hole feedback”, *MNRAS*, **490**, 3234
- Noeske K. G. et al., 2007, “Star Formation in AEGIS Field Galaxies since $z=1.1$: The Dominance of Gradually Declining Star Formation, and the Main Sequence of Star-forming Galaxies”, *ApJ*, **660**, L43
- Olver F. W. J., Lozier D. W., Boisvert R. F., Clark C. W., 2010, *NIST Handbook of Mathematical Functions*, Cambridge Univ. Press, Cambridge
- Oser L., Ostriker J. P., Naab T., Johansson P. H., Burkert A., 2010, “The Two Phases of Galaxy Formation”, *ApJ*, **725**, 2312
- Pillepich A. et al., 2018, “First results from the IllustrisTNG simulations: the stellar mass content of groups and clusters of galaxies”, *MNRAS*, **475**, 648
- Pillepich A. et al., 2019, “First results from the TNG50 simulation: the evolution of stellar and gaseous discs across cosmic time”, *MNRAS*, **490**, 3196
- Poci A., Cappellari M., McDermid R. M., 2017, “Systematic trends in total-mass profiles from dynamical models of early-type galaxies”, *MNRAS*, **467**, 1397
- Poci A., McDermid R. M., Zhu L., van de Ven G., 2019, “Combining stellar populations with orbit-superposition dynamical modelling: the formation history of the lenticular galaxy NGC 3115”, *MNRAS*, **487**, 3776
- Rantala A., Rawlings A., Naab T., Thomas J., Johansson P. H., 2024, “The supermassive black hole merger-driven evolution of high-redshift red nuggets into present-day cored early-type galaxies”, *MNRAS*, **535**, 1202
- Rousseeuw P., Van Driessen K., 2006, “Computing LTS Regression for Large Data Sets”, *Data Mining and Knowledge Discovery*, **12**, 29
- Rusli S. P. et al., 2013, “The Influence of Dark Matter Halos on Dynamical Estimates of Black Hole Mass: 10 New Measurements for High- σ Early-type Galaxies”, *AJ*, **146**, 45
- Rybicki G. B., 1987, “Deprojection of Galaxies - how much can BE Learned”, *Structure and Dynamics of Elliptical Galaxies*, p. 397
- Sandage A., 2005, “The Classification of Galaxies: Early History and Ongoing Developments”, *ARA&A*, **43**, 581
- Sandage A., 1961, *The Hubble Atlas of Galaxies*, Carnegie Institution of Washington, Washington
- Santucci G. et al., 2022, “The SAMI Galaxy Survey: The Internal Orbital Structure and Mass Distribution of Passive Galaxies from Triaxial Orbit-superposition Schwarzschild Models”, *ApJ*, **930**, 153
- Schawinski K. et al., 2014, “The green valley is a red herring: Galaxy Zoo reveals two evolutionary pathways towards quenching of star formation in early- and late-type galaxies”, *MNRAS*, **440**, 889
- Schwarzschild M., 1979, “A numerical model for a triaxial stellar system in dynamical equilibrium”, *ApJ*, **232**, 236
- Scott N., Davies R. L., Houghton R. C. W., Cappellari M., Graham A. W., Pimblet K. A., 2014, “Distribution of slow and fast rotators in the Fornax cluster”, *MNRAS*, **441**, 274
- Scott N. et al., 2017, “The SAMI Galaxy Survey: global stellar populations on the size-mass plane”, *MNRAS*, **472**, 2833
- Sérsic J. L., 1968, *Atlas de galaxias australes*, Obs. Astron. Univ. Nacional de Córdoba, Córdoba
- Shapiro K. L., Cappellari M., de Zeeuw T., McDermid R. M., Gebhardt K., van den Bosch R. C. E., Statler T. S., 2006, “The black hole in NGC 3379: a comparison of gas and stellar dynamical mass measurements with HST and integral-field data”, *MNRAS*, **370**, 559
- Skibba R. A., Bamford S. P., et al., 2009, “Galaxy Zoo: disentangling the environmental dependence of morphology and colour”, *MNRAS*, **399**, 966

- Somerville R. S., Davé R., 2015, “Physical Models of Galaxy Formation in a Cosmological Framework”, *ARA&A*, **53**, 51
- Spiniello C., Trager S. C., Koopmans L. V. E., Chen Y. P., 2012, “Evidence for a Mild Steepening and Bottom-heavy Initial Mass Function in Massive Galaxies from Sodium and Titanium-oxide Indicators”, *ApJ*, **753**, L32
- Stanford S. A., Eisenhardt P. R., Dickinson M., 1998, “The Evolution of Early-Type Galaxies in Distant Clusters”, *ApJ*, **492**, 461
- Strateva I. et al., 2001, “Color Separation of Galaxy Types in the Sloan Digital Sky Survey Imaging Data”, *AJ*, **122**, 1861
- Syer D., Tremaine S., 1996, “Made-to-measure N-body systems”, *MNRAS*, **282**, 223
- Thomas J., Saglia R. P., Bender R., Erwin P., Fabricius M., 2014, “The Dynamical Fingerprint of Core Scouring in Massive Elliptical Galaxies”, *ApJ*, **782**, 39
- Thomas J. et al., 2009, “The flattening and the orbital structure of early-type galaxies and collisionless N-body binary disc mergers”, *MNRAS*, **393**, 641
- Treu T., Auger M. W., Koopmans L. V. E., Gavazzi R., Marshall P. J., Bolton A. S., 2010, “The Initial Mass Function of Early-Type Galaxies”, *ApJ*, **709**, 1195
- Trujillo I., Erwin P., Asensio Ramos A., Graham A. W., 2004, “Evidence for a New Elliptical-Galaxy Paradigm: Sérsic and Core Galaxies”, *AJ*, **127**, 1917
- Trujillo I. et al., 2006, “The Size Evolution of Galaxies since $z \sim 3$: Combining SDSS, GEMS, and FIRES”, *ApJ*, **650**, 18
- Van den Bergh S., 1976, “A new classification system for galaxies”, *ApJ*, **206**, 883
- Van der Wel A. et al., 2014, “3D-HST+CANDELS: The Evolution of the Galaxy Size-Mass Distribution since $z = 3$ ”, *ApJ*, **788**, 28
- Van der Wel A. et al., 2022, “The Mass Scale of High-redshift Galaxies: Virial Mass Estimates Calibrated with Stellar Dynamical Models from LEGA-C”, *ApJ*, **936**, 9
- Van de Sande J. et al., 2021a, “The SAMI Galaxy Survey: a statistical approach to an optimal classification of stellar kinematics in galaxy surveys”, *MNRAS*, **505**, 3078
- Van de Sande J. et al., 2021b, “The SAMI galaxy survey: Mass and environment as independent drivers of galaxy dynamics”, *MNRAS*, **508**, 2307
- Van Dokkum P. G., Conroy C., 2010, “A substantial population of low-mass stars in luminous elliptical galaxies”, *Nature*, **468**, 940
- Van Dokkum P. G., Franx M., Fabricant D., Illingworth G. D., Kelson D. D., 2000, “Hubble Space Telescope Photometry and Keck Spectroscopy of the Rich Cluster MS 1054-03: Morphologies, Butcher-Oemler Effect, and the Color-Magnitude Relation at $z = 0.83$ ”, *ApJ*, **541**, 95
- Van Dokkum P. G. et al., 2010, “The Growth of Massive Galaxies Since $z = 2$ ”, *ApJ*, **709**, 1018
- Vázquez-Mata J. A. et al., 2022, “SDSS IV MaNGA: visual morphological and statistical characterization of the DR15 sample”, *MNRAS*, **512**, 2222
- Veale M., Ma C.-P., Greene J. E., Thomas J., Blakeslee J. P., McConnell N., Walsh J. L., Ito J., 2017, “The MASSIVE Survey - VII. The relationship of angular momentum, stellar mass and environment of early-type galaxies”, *MNRAS*, **471**, 1428
- Virtanen P. et al., 2020, “SciPy 1.0: fundamental algorithms for scientific computing in Python”, *Nature Methods*, **17**, 261
- Wang B., Cappellari M., Peng Y., 2021, “Physical explanation for the galaxy distribution on the (λ_R, ϵ) and $(V/\sigma, \epsilon)$ diagrams or for the limit on orbital anisotropy”, *MNRAS*, **500**, L27
- Wang B., Cappellari M., Peng Y., Graham M., 2020, “SDSS-IV MaNGA: The kinematic-morphology of galaxies on the mass versus star-formation relation in different environments”, *MNRAS*, **495**, 1958
- Wang B., Peng Y., Cappellari M., Gao H., Mo H., 2024, “On the Kinematic Nature of Apparent Disks at High Redshifts: Local Counterparts are Not Dominated by Ordered Rotation but by Tangentially Anisotropic Random Motion”, *ApJ*, **973**, L29
- Weijmans A.-M. et al., 2014, “The ATLAS^{3D} project - XXIV. The intrinsic shape distribution of early-type galaxies”, *MNRAS*, **444**, 3340
- White S. D. M., Rees M. J., 1978, “Core condensation in heavy halos - A two-stage theory for galaxy formation and clustering”, *MNRAS*, **183**, 341
- Wyithe J. S. B., Turner E. L., Spergel D. N., 2001, “Gravitational Lens Statistics for Generalized NFW Profiles: Parameter Degeneracy and Implications for Self-Interacting Cold Dark Matter”, *ApJ*, **555**, 504
- Zhu K., Lu S., Cappellari M., Li R., Mao S., Gao L., 2023, “MaNGA DynPop - I. Quality-assessed stellar dynamical modelling from integral-field spectroscopy of 10K nearby galaxies: a catalogue of masses, mass-to-light ratios, density profiles, and dark matter”, *MNRAS*, **522**, 6326
- Zhu K., Lu S., Cappellari M., Li R., Mao S., Gao L., Ge J., 2024, “MaNGA DynPop - III. Stellar dynamics versus stellar population relations in 6000 early-type and spiral galaxies: Fundamental Plane, mass-to-light ratios, total density slopes, and dark matter fractions”, *MNRAS*, **527**, 706